

GROUND STATE AND
EXCITATIONS OF THE SPIN
 $\frac{1}{2}$ KAGOMÉ LATTICE

LITAL MARCIPAR GOLDSTEIN

The Research Thesis Was Done Under The Supervision of
Prof. Amit Keren
in the Faculty of Physics

Acknowledgements

I would like to thank Prof. Amit Keren for the opportunity to integrate in his fascinating research. I am deeply grateful for the excellent guidance throughout this period.

I thank Dr. Ravi Chandra and Dr. Daniel Podolsky for their tremendous help in theoretical calculations.

I thank Dr. Aharon Blank and Dr. Boris Tumansky, from the Chemistry faculty, for the help in the ESR experiment. I thank all my friends in the research group of magnetism and low temperatures for their help and for the time we spent together.

I thank my family, and a special thanks to Menachem, my husband, for their infinite love and support.

The Generous Financial Help of the Technion is Gratefully
Acknowledged

Contents

Acknowledgements	i
List of Tables	iii
List of Figures	iv
Abstract	1
Symbols	2
1 Introduction	4
1.1 Cu(1,3-bdc) Compound	7
2 Experimental Methods	9
2.1 Susceptibility Measurements	9
2.2 ESR	10
2.2.1 ESR spectrometer	11
2.2.2 Continuous Wave ESR	13
2.3 μ SR	15
2.3.1 Transverse Field Configuration	17
2.3.2 Longitudinal Field Configuration	19
3 Results	24
3.1 Susceptibility measurements	24
3.2 ESR	29
3.3 μ SR	30
3.3.1 TF μ SR	31
3.3.2 LF μ SR	35
4 Discussion	37
4.1 Susceptibility in an anisotropic spin Hamiltonian	37
4.2 ESR linewidth in terms of moments	40
4.2.1 Hamiltonian parameters	47
4.3 μ SR result against theory	48
5 Conclusions	50

List of Tables

2.1	Typical frequencies for ESR experiment.	12
4.1	Numerical solutions for the spin Hamiltonian parameters.	47

List of Figures

1.1	Spins arrangement in a square lattice	4
1.2	Spins arrangement in a triangle lattice	5
1.3	The kagomé lattice - a lattice of corner sharing triangle	6
1.4	The Cu(1,3-bdc) structure showing the Kagomé planes, the inter-plane and intra-plane superexchange path	8
1.5	Cu(1,3-bdc) crystalline picture	8
2.1	Zeeman splitting	11
2.2	ESR absorption and first derivation lines	15
2.3	Angular distribution of emitted positrons	16
2.4	Schematic of a transverse-field μ SR configuration	17
2.5	Schematic of zero-field μ SR configuration	20
2.6	Muon polarization function in a Gaussian internal field distribution and external field pointing in the initial muon spin direction	22
2.7	The muon spin polarization in the ZF μ SR with a dynamic and Gaussian internal field distribution	23
3.1	Preparation for SQUID anisotropy experiments	25
3.2	High temperature susceptibility for several fields parallel to the kagomé plane	26
3.3	High temperature susceptibility for several fields perpendicular to the kagomé plane	26
3.4	Inverse susceptibility measured at 100 Oe	27
3.5	Magnetization vs the magnetic field	27
3.6	ESR absorption lines for the Cu(1,3-bdc) compound at 295 K	29
3.7	Temperature dependence of the linewidth, intensity and g-factor	30
3.8	FFT of the asymmetry data in a field of 1 kOe transverse to the initial muon spin direction	32
3.9	Muon shift and relaxation rate against temperature	33
3.10	Magnetization and muon relaxation versus the muon shift in Cu(1,3-bdc)	34
3.11	Longitudinal and zero field μ SR data	36
3.12	Fluctuation rate ν vs temperature	36
4.1	One dimensional spins chain	44
4.2	Two dimensional triangle bonds	45

4.3	The numerical relaxation, Γ_a compered with ν exhibit a linear function of the temperature.	48
-----	----------------------------------------------------------------------------------------------------------------	----

Abstract

The experimental search for an ideal two dimensional, spin 1/2, Kagomé compound, which has no out-of-plane interactions and no impurities on the Kagomé plane, has powered tremendous experimental efforts in recent years. Recently a new Kagomé compound was synthesized. New organometallic hybrid compound Cu(1,3-benzendicarboxylate) [Cu(1,3-bdc)], which has structurally spin 1/2 copper kagomé planes separated by pure organic linkers. Using muon spin resonance (μSR), magnetization measurements and electron spin resonance (ESR) we examine this new Kagomé. Susceptibility and ESR measurements revealed distinct anisotropy behavior. By orienting the sample two different θ_{cw} are found. When the applied external field is parallel to the Kagomé planes, θ_{cw}^z exhibits ferromagnetic interactions. As for the perpendicular direction, θ_{cw}^\perp is not reliable, thus we cannot characterize the interactions in the Kagomé planes from magnetization measurements alone. Furthermore, ESR measurements done on the Cu(1,3-bdc) compound reinforced the presence of anisotropy. We get two different g-factors for each direction measured and two different ESR line-widths, which were found out to be temperature independent. Susceptibility and ESR measurements combined with theoretical calculations allow us to characterize the spin Hamiltonian.

From the μSR experiment we found slowing down of spin fluctuations starting at $T = 1.8$ K, and that the state at $T \rightarrow 0$ is quasi-static with no long-range order and extremely slow spin fluctuations at a rate of $3.6\mu sec^{-1}$. This indicates that Cu(1,3-bdc) behaves as expected from a Kagomé compound.

Symbols

AFM	Antiferromagnetic
HWHI	Half Width Half Intensity
DMI	Dzaloshinsky-Moriya Interaction
bdc	Benzendicarboxylate
n.n	Nearest-neighbor interaction
Bg	Background
T	Temperature
J	Exchange coupling constant
S	Electronic spin
I	The muon spin
H	External magnetic Field
B	Internal local magnetic field
g	g-factor
μ_B	Bohr Magneton
\mathcal{D}	Dzaloshinsky-Moriya vector
θ_{CW}	Currie-Weiss Temperature
C	Currie-Weiss constant
k_B	Boltzman constant
K	Muon's shift
R	Muon's relaxation
z	Number of near neighbors
$A_k(r)$	Hyperfine coupling
ϵ	Normalized energy

ω	Angular frequency
P_μ	Muon polarization
γ	Gyromagnetic ratio
\hbar	Plank constant
η	Filling factor
Q	Quality factor
Q_0	Unloaded quality factor
χ''	Imaginary part of a susceptibility
Δ	Field distribution width
ν	Spin fluctuation rate
δ	Half width half intensity of electron spin absorption line

Chapter 1

Introduction

In most magnetic materials at high temperature regime the spins (due to the presence of unpaired electrons) are subject to thermal agitation and are random in orientation, a state called paramagnetism. As the temperature is lowered spin-spin interactions eventually dominate the thermal energy and the spins can lower their energy by aligning or ordering with each other. The most common ordering is that in which the nearest neighbor (n.n.) spins align antiparallel (antiferromagnetically) as in Fig. 1.1 where the spins are on the corners of a square. In this geometry there is no impediment to the establishment of n.n. spin order. Consider now the case of

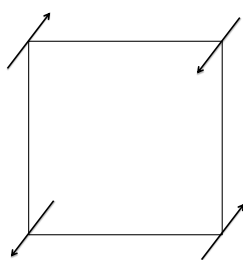


FIGURE 1.1: Spins arrangement in a square lattice.

Fig. 1.2, where the spins are on the corners of an equilateral triangle. Here there is a strong geometric impediment to spin ordering as only two of the three spins can be aligned antiparallel simultaneously. The combination of triangle-based lattice symmetry and antiferromagnetism results in phenomena known as geometrical frustration, which has attracted much interest in the last two decades. Frustration

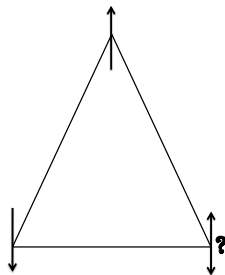


FIGURE 1.2: Spins arrangement in a triangle lattice.

is the inability of a system to simultaneously minimize the total energy of its classical ground state by minimizing individual microscopic interactions. Highly frustrated magnets have a large degenerate ground state. Heisenberg Hamiltonian describing the interaction between n.n. spins is,

$$\mathcal{H} = J \sum_{\langle i,j \rangle} S_i \cdot S_j \quad (1.1)$$

where J is the exchange coupling constant, $J > 0$ is the antiferromagnetic (AFM) exchange and the sum $\langle i, j \rangle$ is over all n.n. spins. Considering a triangle lattice with n.n. interactions, the energy is minimized for collinear (parallel or antiparallel) spin alignments. Under the condition that J is positive which favors the AFM correlation, the system is geometrically frustrated. Frustrated magnets include the two dimensional (2D) kagomé lattice (see Fig. 1.3), which is a lattice of corner sharing triangle, and its big brother, the 3D pyrochlore, a lattice of corner sharing tetrahedra. A kagomé AFM presents an ideal construct for studying the unusual physics that result from the placement of magnetically frustrated spins on a low-dimensional lattice. Tremendous efforts are invested to find the perfect candidate for studying the ground state of 2D kagomé lattice. A two dimensional compound which has spin 1/2, no out-of-plane interactions and no impurities on the kagomé plane. The search for kagomé realization led to various new materials, synthesized especially for this purpose.

The $SrCr_xGa_{12-x}O_{19}$ [SCGO] compound, a kagomé lattice with $S = 3/2$, which may behave classically. The SCGO found to have alternating magnetic planes with kagomé and triangle lattices and that Ga atoms, which are non magnetic,

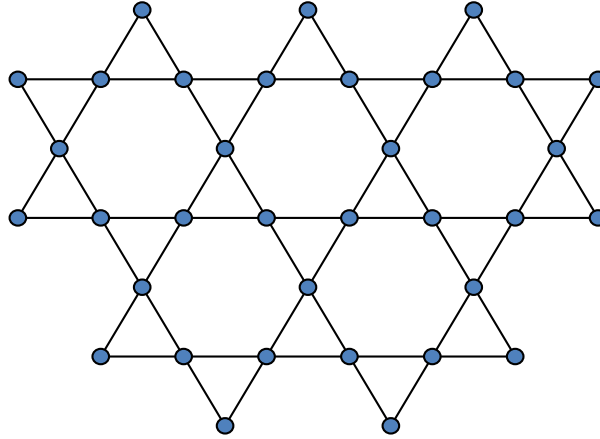


FIGURE 1.3: The kagomé lattice - a lattice of corner sharing triangle partly substitute magnetic Cr sites [1, 2].

The volborthite compound, $Cu_3V_2O_7(OH)_2 \cdot 2H_2O$, 2D AFM spin 1/2 kagomé comprising two different sites of Cu . Thus, the kagomé lattice is slightly distorted [3].

Another candidates is the jarosite family, $KA_3(OH)_6(SO_4)_2$, where $A = Fe, Cr$. The Fe-jarosite Fe^{3+} , $S = 5/2$, exhibits long-range order in the ground state. As for the Cr-jarosite Cr^{3+} , $S = 3/2$, may involve large effect of quantum fluctuations [2].

The vesignieite, $BaCu_3V_2O_8(OH)_2$, comprising a nearly ideal kagomé lattice of Cu^{2+} ions with spin 1/2 and impurity contribution were found at low temperature susceptibility measurements [4].

Another two less investigated compounds are the Kapellasite, $Cu_3Zn(OH)_6Cl_2$, and the Haydeeite, $Cu_3Mg(OH)_6Cl_2$, seem to have defects on the kagomé plane [5, 6].

The discovery of Herbertsmithite, $ZnCu_3(OH)_6Cl_2$, thought to be the end of the research after kagomé realization. It has no long-range-order and strong AFM interactions, However, further measurements done on it revealed a not so perfect compound. About 10% of the Cu_{2+} sites in the Kagomé plane are substitute by Zn^{2+} ions [7–9].

None of those compounds are good enough to be elected as the perfect Kagomé

model. Recently a new Kagomé compound was synthesized by Nytko *et al.* [10], The Cu(1,3-bdc).

1.1 Cu(1,3-bdc) Compound

The Cu(1,3-bdc) compound is a copper-based organometallic compound with spin $1/2$. It was synthesized by Nytko *et al.* [10]. An ideal Kagomé lattice structure was determined by X-ray measurements. As oppose to the Herbertsmithite, this compound doesn't have Zn ions, or any other candidate, which can substitute the Cu ions on the Kagomé plane.

Cu(1,3-bdc) is shorthand for Cu(1,3-benzendicarboxylate). The Kagomé planes are separated by organic linkers, each linker being a benzen molecule with two corners featuring a carboxylate ion instead of the standard hydrogen ion. By labeling each corner of the benzen molecule, one can see that the two corners with the carboxylate ions would be the 1st and 3rd. The superexchange path of Cu ions located on the plane is shorter than the superexchange path of Cu ions between the plane. This indicates a 2D Kagomé compound.

The basic elements of Cu(1,3-bdc) are depicted in Fig. 1.4.

The powder contains blue crystalline plates which are the Cu(1,3-bdc) and green spheres which are a copper-containing ligand oxidation byproduct $C_{32}H_{24}Cu_6O_{26}$, see Fig. 1.5. Magnetization measurements, done on the powder, found antiferromagnetic $\theta_{cw} = -33$ K. Heat capacity shows a peak at $T \simeq 2K$ [10].

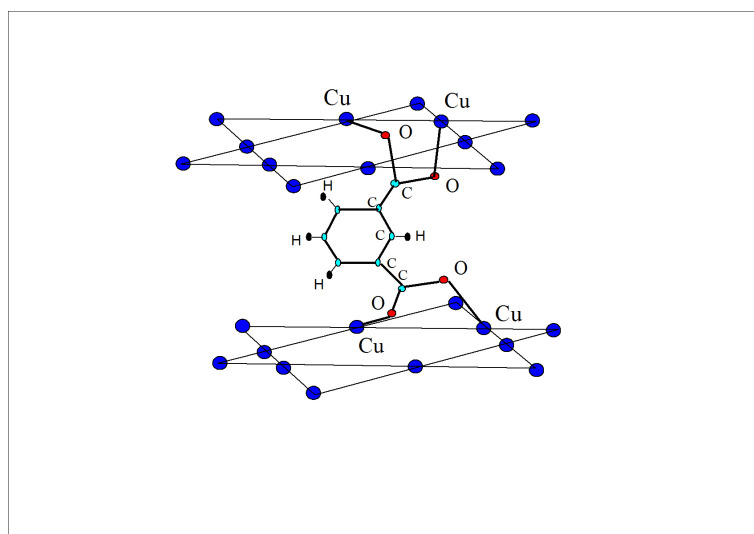


FIGURE 1.4: The Cu(1,3-bdc) structure showing the Kagomé planes, the inter-plane and intra-plane superexchange path.

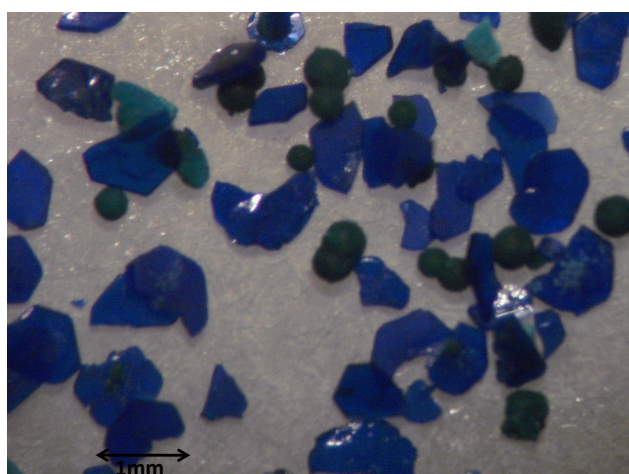


FIGURE 1.5: Blue plates: large single crystals of Cu(1,3-bdc). Green spheres: a copper-containing ligand oxidation byproduct $C_{32}H_{24}Cu_6O_{26}$.

Chapter 2

Experimental Methods

In this chapter we describe three different techniques used to examine the Cu(1,3-bdc) kagomé compound. We begin with an introduction to susceptibility measurements, continue with Electron Spin Resonance (ESR) experiment. Finally, we will describe μ SR experiment considering its three possible configurations: Transverse-Field(TF), Longitudinal-Field(LF) and Zero-Field(ZF) μ SR.

2.1 Susceptibility Measurements

Superconducting Quantum Interference Device (SQUID) is one of the most sensitive magnetometers. The SQUID magnetometer uses the interaction between magnetic flux and Josephson junction. Magnetic flux modulates the current passing through the junction. This modulation is detected and amplified by some feedback electronics. There are two types of SQUIDs, AC (or RF) and DC SQUIDs. Our measurements were done with a dc-SQUID. The dc-SQUID, which operates with a dc bias current, consists of two parallel Josephson junctions incorporated into a superconducting loop. The measurements in the Cryogenic SQUID are performed by moving the sample through a coil from its upper to its lower part and back. A change in the magnetic flux occurs when the sample moves through the

coil. This movement induces screening current in the coil, which is proportional to the induced magnetic moment of the sample and is detected by the SQUID.

2.2 ESR

ESR is a branch of spectroscopy in which electromagnetic radiation (usually of microwave frequency) is absorbed by molecules, ions, or atoms possessing electrons with unpaired spins, *i.e.* electronic spin $S > 0$.

The basic physical concepts of ESR are analogous to those of nuclear magnetic resonance (NMR), but it is electron spins that are excited instead of spins of atomic nuclei. Electrons usually occupy electronic shells in atoms as pairs. In such pairs the electrons have spins opposite one another so the associated magnetic fields cancel.

In some ions, free radicals or paramagnetic materials, however, a single electron may occupy an orbital. In both ESR and NMR, the sample material is immersed in a strong static magnetic field and exposed to an orthogonal low-amplitude high-frequency field.

ESR usually requires microwave-frequency radiation (GHz), while NMR is observed at lower radio frequencies (MHz). With ESR, energy is absorbed by the sample when the frequency of the radiation is appropriate to the energy difference between two states of the electrons in the sample, but only if the transition satisfies the appropriate selection rules. In the case where no magnetic field is applied, the 2 energy states of the electron are degenerate. By applying an external magnetic field, B_0 , those electron energy states, split into two energy levels as depicted in Fig. 2.1, and the separation between the levels is

$$\Delta E = g_e \mu_B B_0 \quad (2.1)$$

where g_e is the electron's g-factor and μ_B is the Bohr magneton. This interaction, known as the Zeeman interaction. ESR signal can be obtained by two types of spectrometers, continuous wave (CW) ESR and pulsed ESR spectrometer. In CW

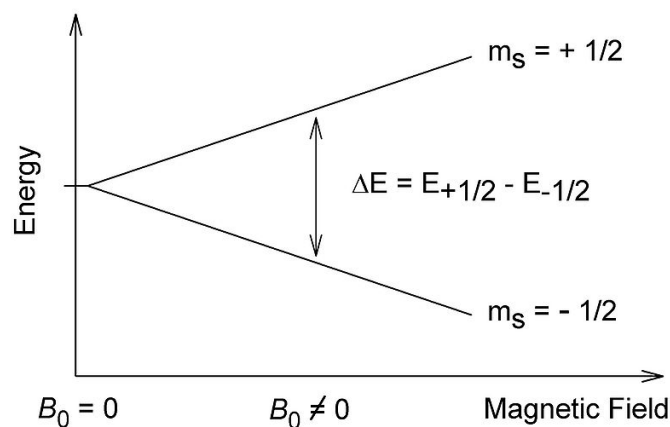


FIGURE 2.1: Energy level scheme for the simplest system (*e.g.*, free electron) as a function of applied magnetic field B .

ESR, a constant electromagnetic radiation is applied and the external magnetic field (B_0) is swept. When the resonance condition occurs, ESR signal can be detected.

In pulsed ESR, the external magnetic field is fixed and by applying an electromagnetic pulse, which enables excitation of a range of frequencies in the sample, ESR signal can be detected. We used the CW technique in our ESR experiment. We shall describe briefly the principal components of a simple ESR spectrometer.

2.2.1 ESR spectrometer

The simplest type of ESR spectrometer consists basically of a microwave source, a sample cell or a cavity and a detector. The electromagnetic source and the detector are in a box called the microwave bridge. The sample is in a microwave cavity, which is a metal box that helps to amplify weak signals from the sample.

Source.

Most common frequency of radiant energy used in ESR spectrometer is in the medium frequency microwave regime, ~ 9.5 GHz. In the microwave region ($1 \leq \nu \leq 100$ GHz) various special electromagnetic radiation sources can be used. These include gunn-diodes, tunnel-diodes, voltage control oscillators, klystron etc.

Frequencies typical for ESR experiment are from 1.5 GHz to 250 GHz as seen in

table 2.1. Our ESR experiment was performed in the X-band regime.

Magnetic field (Tesla)	Typical frequency (GHz)	Band region
0.05	1.5	L
0.12	3.2	S
0.35	9.5	X
1.29	35	F(W)
5.54	150	G(A)
9.25	250	H

TABLE 2.1: Typical frequencies for ESR experiment.

Resonator.

The heart of a typical ESR spectrometer is a device called a resonator, which contains the sample. This is most commonly a resonant cavity. The cavity is a closed box made of a conducting material, which confines standing electromagnetic waves with wavelength that matches the cavity dimensions. Resonance means that the cavity stores the microwave energy; therefore, at the resonance frequency of the cavity, no microwaves will be reflected back, but will remain inside the cavity. Cavities are characterized by Q , the quality factor, which indicates how efficiently the cavity stores microwave energy. As Q increases the sensitivity of the spectrometer increases. The Q factor is defined as,

$$Q = 2\pi \frac{\text{energy stored}}{\text{energy dissipated per cycle}}$$

where the energy dissipated per cycle is the amount of energy lost during one microwave period. We couple the microwaves into the cavity via a hole called iris. An adjustable screw adjacent to the iris permits optimal impedance matching. The frequency of the source is tuned to the appropriate resonant frequency of the cavity. The size of the iris controls the amount of microwaves which will be reflected back from the cavity and how much will enter the cavity. When the sample absorbs the microwave energy, the Q is lowered because of the increased losses and the coupling changes because the absorbing sample changes the impedance of the cavity. The cavity is therefore no longer critically coupled and microwaves will be

reflected back to the bridge, resulting in an ESR signal.

Detector.

The most common detectors, in CW ESR, is a silicon crystal diodes which detect the absorption of energy. Absorption lines can be observed in the ESR spectrum when the separation of two energy levels is equal to the quantum energy $h\nu$ of an incident microwave photon. The absorption of such photons by the sample is indicated by a change in the detector current. This current is proportional to the microwave power. The noise figure of a particular crystal detector varies with frequency, temperature and power level. Disadvantage of the crystal detector is production of inherent noise which is proportional to the reciprocal of the frequency of the detected signal. To reduce noise a locking amplifier is used.

Magnetic Field.

The usual source of static magnetic field B , which polarized and splits the spin energy levels, is an electromagnet or a superconductor magnet for fields higher than 2 T. This external field must be uniform over the sample volume and stable during the measurement.

2.2.2 Continuous Wave ESR

In CW ESR, the sample is being continuously irradiated by microwave radiation. The resonator reflects power back to the transmission line feeding it, as it is well matched to the microwave power source. We measure the reflected power without the sample minus the reflected power with the sample. This gives the absorbed power P . There are two external parameters in ESR, the frequency ω and the magnetic field H which is swept. Since the frequency is fixed we can write the energy absorbed as follows [11, 12]

$$\frac{\Delta P_c}{P_w} \simeq \chi'' \eta Q_u \quad (2.2)$$

where ΔP_c is the change in reflected power, P_w is the maximum power supplied from the source, Q_u is the unloaded quality factor, χ'' imaginary part of the susceptibility and η the filling factor. The filling factor is defined by,

$$\eta = \frac{\int_{V_s} B_1^2 dV}{\int_{V_c} B_1^2 dV}$$

B_1 is the microwave magnetic field, V_s is the sample volume and V_c is the cavity volume [12]. Q_u and the filling factor η are related to the cavity geometry. Up to a calibration constant ESR signal is $\chi''(H, \omega)$. In order to improve sensitivity a modulation field is added,

$$H = St + H_1 \cos(\omega_a t) \quad (2.3)$$

where S is the sweeping rate (field per time), and S is much smaller than ω_a . Therefore, at a given time we can expand χ'' to series as follows,

$$\chi''(H, \omega) = \chi''(St, \omega) + \frac{\partial \chi''(H, \omega)}{\partial H} H_1 \cos(\omega_a t) \quad (2.4)$$

H_1 is a fixed number for experiment. A lockin detects the amplitude of the fast modulations in the absorption power, therefore the ESR signal is

$$\frac{\partial \chi''(H, \omega)}{\partial H}$$

as seen in Fig. 2.2. To obtain $\chi''(H, \omega)$ up to a calibration constant the ESR signal as a function of H should be integrated once. $\chi''_{\alpha\beta}(H, \omega)$ has a peak when

$$\omega_0 = g\mu_B H.$$

Another way to describe the absorption line is by a Lorentzian/Gaussian function. Using the method of moments of a resonance curve we will demonstrate in Chapter 4.2 the connection between χ'' and the fitted function. The method of moments allow us to connect between experiment and theory.

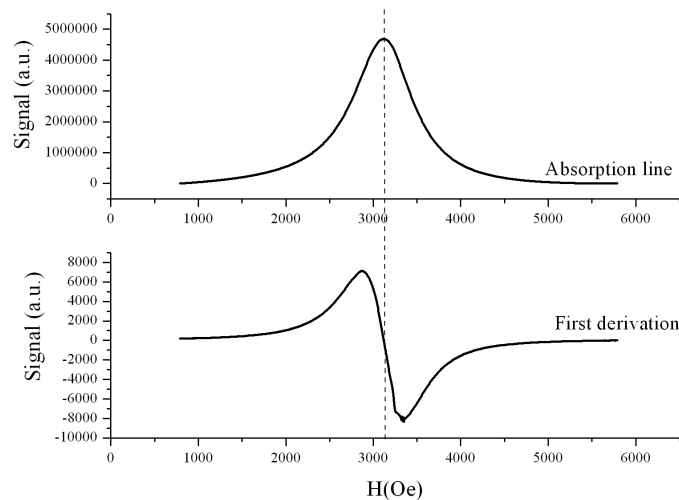
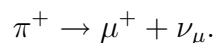


FIGURE 2.2: Absorption and first derivation lines of an ESR spectrum.

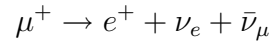
2.3 μ SR

Muon spin rotation, relaxation, resonance and etc. (μ SR) is an experimental technique used for basic studies in condensed matter physics. This technique makes use of a short-lived subatomic particle of the lepton family called a muon, the muon is a sensitive probe of local magnetic fields in matter. Muons are charged (μ^+ , in our case or μ^-) spin 1/2 particles. High energy proton beams (produced using synchrotrons or cyclotrons) can be fired into a target (usually carbon) to produce pions. The pions decay into muons, as follows:



Consider pions that are produced at rest in the laboratory frame. To conserve momentum, the muon and the neutrino must have equal and opposite momentum. The neutrinos spin is aligned antiparallel with its momentum (it has negative helicity). The pion has zero spin so the muon spin must be opposite to the neutrino spin, and this implies that the muon-spin is similarly aligned. By selecting pions which stop in the target (and which are therefore at rest when they decay) one has a means of producing a beam of 100% spin-polarized muons. The muon is an unstable particle which decays spontaneously into a positron (or an electron) and

a neutrino-anti-neutrino pair:



its mean-life time is $\tau_\mu \simeq 2.2\mu\text{ sec}$.

The positrons are emitted preferentially in the muon spin direction. The angular distribution of the emitted positrons (see Fig. 2.3) depends on their energies and is given by:

$$W(\theta, \epsilon) = 1 + a(\epsilon) \cos \theta$$

where ϵ is the positron energy and θ is the angle of the positron emission measured from the muon spin direction. a is the asymmetry parameter, which depend on the energy of the detected positrons. When both neutrinos are emitted in the same direction, $\epsilon = \epsilon_{max}$ and $a = 1$, when they are emitted in opposite directions, $\epsilon = 0$ and $a = 1/3$. In order to carry out an experiment, the muons are transported

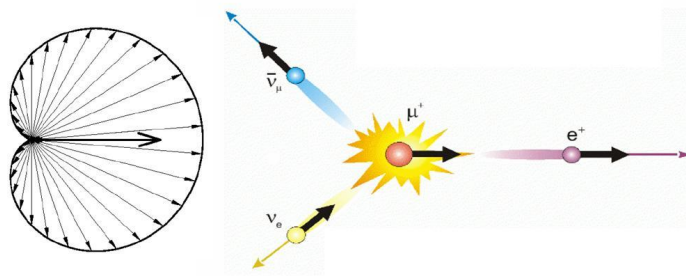


FIGURE 2.3: The angular distribution of emitted positrons.

to the sample using a system of magnets, that conserve spin polarization. The decay positrons are detected using several photomultiplier tubes surrounding the sample. By detecting those positrons we can reconstruct the muon polarization. Each positron detector creates an histogram of detected positrons as a function of the time difference between the muon implantation and the decay positron. The

number of detected positrons in a histogram of detector i is given by,

$$N_i(t) = N_{i0}e^{-t/\tau_\mu} (1 + A_i P_{i\mu}(t)) + B_g$$

where N_{i0} is a normalization, B_g is the time independent background, A_i is the experimental asymmetry and $P_{i\mu}$ is the muon polarization function in the detector. There are different configurations of μ SR experiment depending on how you orient the applied field: zero field, longitudinal field (along the spin polarization), and transverse field (perpendicular to the initial spin polarization). The basic idea is to investigate the nature of the changes in the local environment of the muon as temperature decreases.

2.3.1 Transverse Field Configuration

The simplest μ SR technique (see Fig. 2.4) is the transverse field configuration in which an external magnetic field is applied perpendicular to the initial muon spin polarization, $P_\mu(0)$. Once the muons are implanted into the sample, the muons spin precess at a Larmor frequency, $\omega = \gamma_\mu H$ ($\gamma_\mu = 13.554$ MHz/kG). Hence, $P_\mu(t)$ exhibit oscillation at the Larmor frequency. In order to probe frustrated

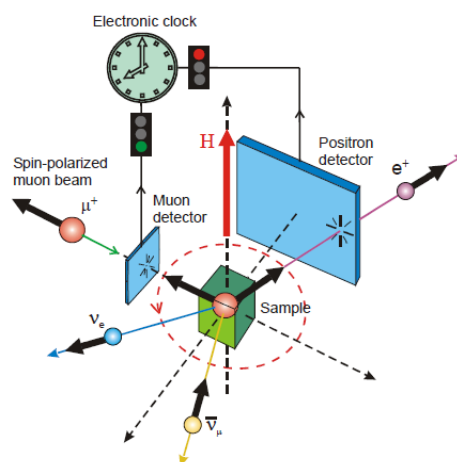


FIGURE 2.4: Schematic of a transverse field (TF) μ SR.

magnetism we look at the Hamiltonian which describes the hyperfine interaction

with the electron spin S . The muon Hamiltonian is:

$$\mathcal{H} = -\hbar\gamma_\mu I \cdot (H_{TF} + H_{\text{int}}) \quad (2.5)$$

I is the muon spin, H_{TF} is the applied field and H_{int} is the magnetic field from neighboring electrons. H_{int} is given by,

$$H_{\text{int}} = \sum_k \tilde{A}_k S_k$$

where $\tilde{A}_k = \tilde{A}_k(r)$ is the hyperfine interaction with each neighboring spin, S_k is the electronic spin. The sum j runs over the muon's neighboring electrons. By a mean field approximation, we replace S by its expectation value $\langle S_k \rangle$.

The field at the muon site is given by

$$B = H - \sum_k \tilde{A}_k \cdot \langle S_k \rangle.$$

Assuming $\langle S_k \rangle \rightarrow \langle S \rangle$ and $\langle S \rangle = M = \chi H$

$$B = H - M \cdot \sum_k \tilde{A}_k \quad (2.6)$$

than we get,

$$\chi \sum_k \tilde{A}_k = \frac{H - B}{H}$$

where $B = \frac{\omega}{\gamma_\mu}$ and $H = \frac{\omega_0}{\gamma_\mu}$. Thus the muon shift is defined as,

$$K = \frac{\langle S \rangle}{H} \sum_k \tilde{A}_k = \frac{\omega_0 - \omega}{\omega_0}. \quad (2.7)$$

Assuming a distribution of hyperfine fields in the \hat{z} direction one can write A_k as a sum of a mean value \bar{A}_k plus a fluctuating component δA_k , $\tilde{A}_k = \bar{A}_k + \delta A_k$.

The transverse muon shift will be,

$$K = \frac{\langle S \rangle}{H} \sum_k \bar{A}_k \quad (2.8)$$

The muon polarization is given by,

$$P_\mu(t) = P_0 \cos[\gamma_\mu B t] = P_0 \cos \left[\gamma_\mu \left(1 - \chi \cdot \sum_k A_k \right) H_{TF} t \right] \quad (2.9)$$

By averaging over the distribution of the fluctuating component,

$$\bar{P}_\mu(t) = \int P_0 \cos \left[\gamma_\mu \left(1 - \chi \cdot \sum_k \bar{A}_k + \delta A_k \right) H_{TF} t \right] \rho(\delta A) d(\delta A) \quad (2.10)$$

considering a Lorentzian distribution

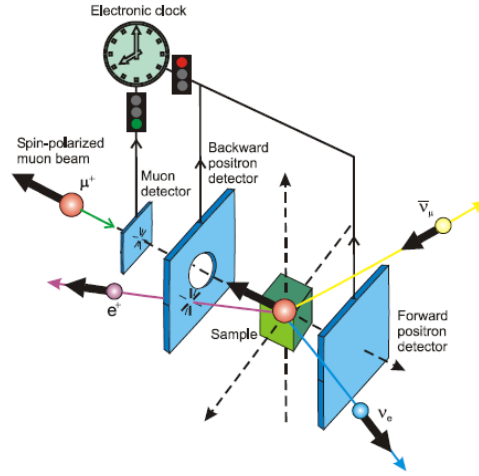
$$\rho(\delta A_k) = \frac{1}{\pi} \frac{\sigma_k}{(\delta A_k)^2 + \sigma_k^2} \quad (2.11)$$

we get the Transverse Field Relaxation [13],

$$R = \gamma_\mu \langle S \rangle \sum_k \sigma_k. \quad (2.12)$$

2.3.2 Longitudinal Field Configuration

Longitudinal Field Muon Spin Relaxation (LF μ SR) involves the application of an external magnetic field parallel to the initial direction of the muon spin polarization. Here one measures the time evolution of the muon polarization along its original direction. Alternatively, such measurements may be performed in the absence of an external field, a configuration called Zero Field Muon Spin Relaxation (ZF μ SR). ZF μ SR is a very sensitive method of detecting weak internal magnetism, that arises due to ordered magnetic moments, or random fields that are static or fluctuating with time.

FIGURE 2.5: Schematic of a zero field (ZF) μ SR.

In order to understand the ZF and LF μ SR experiments we study the time evolution of the muon spin polarization.

For simplicity we start with the static random internal field case. When the implanted muon reaches its site, the muon spin starts to evolve in a local magnetic field B . The static muon polarization along the \hat{z} direction is generated using the double projection expression,

$$P_z(B, t) = \cos^2\theta + \sin^2\theta \cos(\gamma_\mu |B| t) \quad (2.13)$$

The angle θ is connected to the field values by the relations,

$$\cos^2\theta = \frac{B_z^2}{B^2}, \quad \sin^2\theta = \frac{B_x^2 + B_y^2}{B^2}$$

Thus, the averaged polarization is:

$$\bar{P}_z(t) = \int \rho(B) \left[\frac{B_z^2}{B^2} + \frac{B_x^2 + B_y^2}{B^2} \cos(\gamma_\mu |B| t) \right] d^3B \quad (2.14)$$

where $\rho(B)$ is the field distribution. We found that the Gaussian field distribution works best,

$$\rho(B) = \frac{\gamma_\mu^3}{(2\pi)^{3/2} \Delta^3} \exp\left(-\frac{\gamma_\mu^2 [B - H_L]^2}{2\Delta^2}\right) \quad (2.15)$$

where Δ is the field distribution width, H_L is the longitudinal external field and B is the internal local field.

If the field distribution is isotropic, one can integrate over the angular part

$$\bar{P}_z(t) = \frac{1}{3} + \frac{2}{3} \int \rho'(|B|) \cos(\gamma_\mu |B| t) B^2 dB \quad (2.16)$$

In a system with long-range order, which is not expected in 2D Kagomé lattice, the field around the muon site is centered around certain value ω_0/γ_μ and oscillations will be observed. The first term (1/3-component) originates from the fraction of the local field which is parallel to the initial muon spin polarization. This term is an important signature of static relaxation, because its existence doesn't depend on the shape of the field distribution. At long time the polarization will relax to 1/3, in powder.

When a longitudinal field is applied (along the spin polarization), the muon spin will rotate around the vector sum of the external and internal fields.

In order to simplify the LF case, we assume random local field with a Gaussian distribution 2.15. Now Eq. 2.14 becomes [14]:

$$\begin{aligned} \bar{P}_z(\omega_L, \Delta, t) = 1 - \frac{2\Delta^2}{(H_L)^2} \left[1 - \exp\left(-\frac{1}{2}\Delta^2 t^2\right) \cos(H_L t) \right] \\ + \frac{2\Delta^4}{(H_L)^3} \int_0^t \exp\left(-\frac{1}{2}\Delta^2 t'^2\right) \sin(H_L t') dt' \end{aligned} \quad (2.17)$$

This is known as the static-Gaussian longitudinal-field Kubo-Toyabe (KT) function. In Fig. 2.6 plotted the muon spin polarization for several different external fields. In the zero-field case, $H_L = 0$ we get the average polarization [14],

$$\bar{P}_z(0, \Delta, t) = \frac{1}{3} + \frac{2}{3} (1 - \Delta^2 t^2) \exp\left(-\frac{1}{2}\Delta^2 t^2\right) \quad (2.18)$$

Eq. 2.18 is known as the static-Gaussian-zero-field KT. It reaches a minimum on a time scale set by Δ after which it recovers and saturates again to 1/3. The next step is to add dynamics into the system. When the dynamic part of the local field

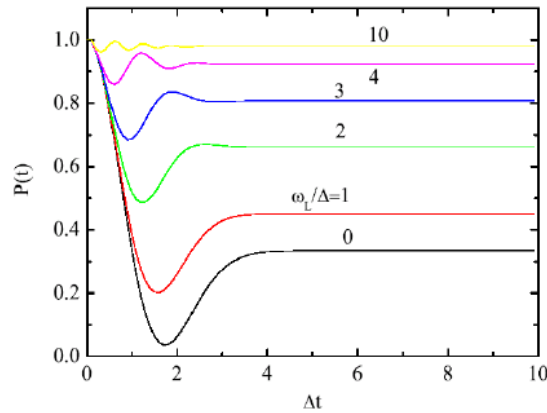


FIGURE 2.6: Muon polarization function in a Gaussian internal field distribution and external field pointing in the initial muon spin direction.

is fluctuating in time, the spin fluctuation rate, ν is defined by

$$\langle B(t) B(0) \rangle = \langle B^2 \rangle e^{-2\nu t}$$

One method of adding dynamics into the system is by using the Volterra equation of the second kind [15],

$$\begin{aligned} \bar{P}_z(\nu, H, \Delta, t) = e^{-\nu t} \bar{P}_z(0, H, \Delta, t) \\ + \nu \int_0^t dt' \bar{P}_z(\nu, H, \Delta, t - t') e^{-\nu t'} \bar{P}_z(0, H, \Delta, t') \end{aligned} \quad (2.19)$$

The $\bar{P}_z(0, H, \Delta, t)$ is the static relaxation function. The factor $e^{-\nu t}$ is the probability to have no field changes up to time t . The factor $e^{-\nu t'} \nu dt'$ is the probability density to experience a field change only between t' and $t' + dt'$. The first term on the r.h.s is the polarization at time t due to muons that did not experienced any field changes. The second term on the r.h.s is the contribution from those muons that experienced their first field change at time t' . The factor $e^{-\nu t'} \bar{P}_z(0, H, \Delta, t') \nu dt'$ is the amplitude for the polarization function evolving from time t' to t , which can include more field changes recursively. This equation can be solved numerically [16] and $\bar{P}_z(\nu, H, \Delta, t)$ is known as the Dynamic Gaussian Kubo Toyabe LF relaxation function. The origin of the dip is the presence of a typical field scale

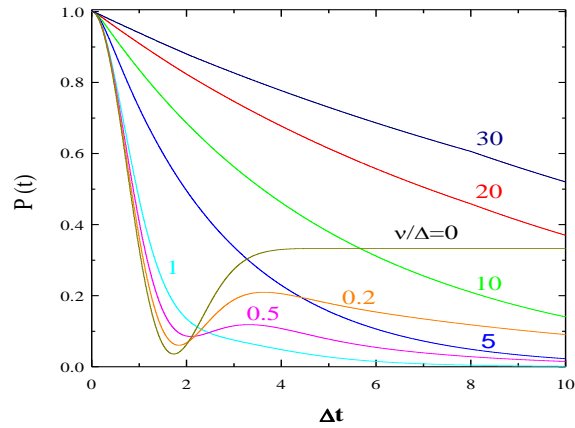


FIGURE 2.7: The muon spin polarization in the ZF μ SR with a dynamic and Gaussian internal field distribution.

around which the muon spin nearly complete an oscillation. However, the field distribution is so wide that the oscillation is damped quickly. The origin of the recovery is the fact that some of the muons experience nearly static field in their initial field direction during the entire measure time. These muons do not lose their polarization while others do. When the external field increases (Fig. 2.6), the dip moves to smaller Δt (as the field scale increase) and the asymptotic value of the asymmetry increases as well (as more muons do not relax).

Chapter 3

Results

In this chapter we present our experimental data and conclusions. First, we will exhibit Susceptibility and ESR results of our kagomé compound. We will continue with result from the μ SR measurements in order to say something physical about the ground state of this Hamiltonian.

3.1 Susceptibility measurements

DC magnetic susceptibility data were collected on crystalline samples, which were glued on a transparency slide, using SQUID magnetometer at temperature ranging from 3.6 K to 304 K and field strength varying from 100 Oe to 24 kOe. The blue plates have a two dimensional nature as can be seen from Fig. 1.5. A single-crystal X-ray diffraction experiment determined that (001), the kagomé plane, is the flat plane of those hexagonal plates [17]. Magnetization measurements were done with the kagomé plane parallel and perpendicular to the field of the SQUID magnet. For magnetization measurements we separate the blue kagomé plates from the green spheres. We glued them with epoxy to a transparency slide and put it in a suitable capsule. For the perpendicular measurements, the slide was standing up in the capsule as seen in Fig. 3.1(b). For the parallel measurements,

the slide was lying in the capsule as seen in Fig. 3.1(a). We also performed measurements of the epoxy in order to reduce it from the raw data depicted in Fig. 3.2 and 3.3. The susceptibility above 50 K show field dependence while below this

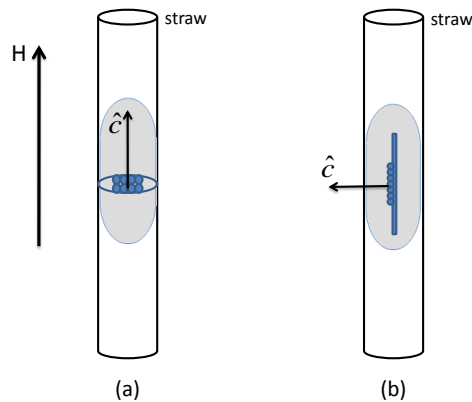


FIGURE 3.1: Preparation for SQUID anisotropy experiments: (a) c-axis parallel to the field of the SQUID magnet. (b) c-axis perpendicular to the field of the SQUID magnet.

temperature there is no field dependence, all susceptibility data merge regardless of the field. In Fig. 3.2 and 3.3 we present the molar susceptibility, at the high temperature regime, for several elected fields in both directions. One can see that the parallel susceptibility is smaller than the perpendicular one. This anisotropy in the magnetic susceptibility means that another Hamiltonian than the Heisenberg Hamiltonian should be used. In the high temperature approximation, the magnetic susceptibility of a ferromagnet is described by Curie-Weiss law,

$$\chi = \frac{C}{T - \theta_{CW}} \quad (3.1)$$

where C is a material-specific Curie constant. In Fig. 3.4 we demonstrate a linear fit for the parallel directions, which reveals

$$\theta_{CW}^{\parallel} = 4.03 \text{ K} \quad (3.2)$$

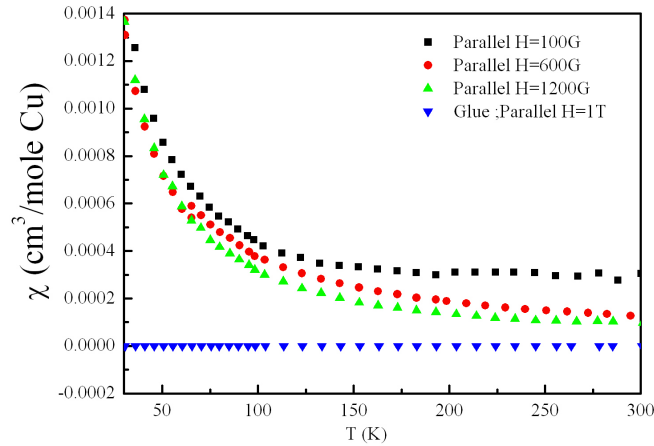


FIGURE 3.2: High temperature susceptibility for several fields parallel to the kagomé plane.

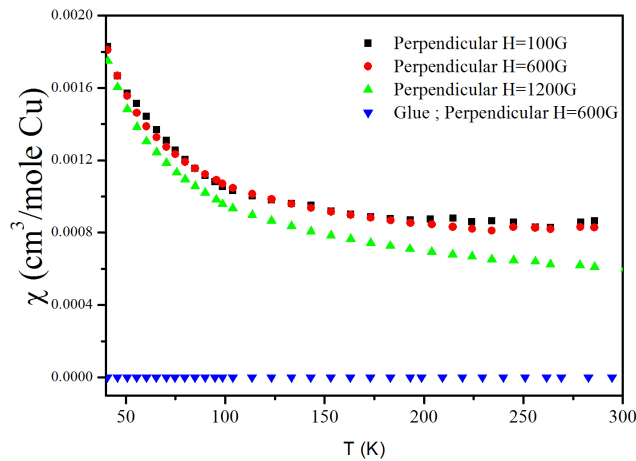


FIGURE 3.3: High temperature susceptibility for several fields perpendicular to the kagomé plane.

The positive θ_{CW} , indicates ferromagnetic interactions in the z direction. The perpendicular directions could not be fitted with a linear fit, thus we don't have value for θ_{CW}^\perp .

In Fig. 3.5 we depicted the magnetization versus the magnetic field measured at $T = 2.4$ K. the magnetization saturates around $1.2 \mu_B/Cu$, hence the g-factor, determine for the parallel and perpendicular directions at low-T, is $g_{\parallel,\perp} \cong 2.5(2)$. The red line in Fig. 3.5 represent a Brillouin function for paramagnetic system

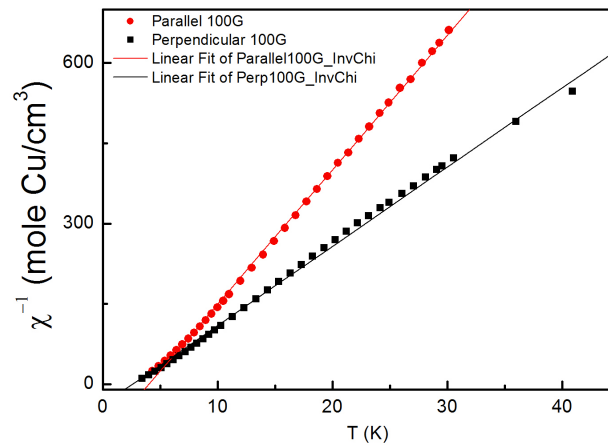


FIGURE 3.4: The inverse susceptibility, measured at 100 Oe. Red line represent linear fit for the data from the 100 Oe parallel field. Black line represent linear fit for the data from the 100 Oe perpendicular field.

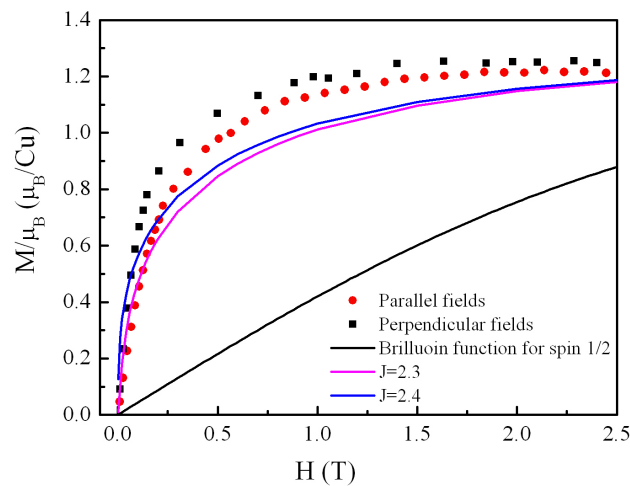


FIGURE 3.5: Magnetization vs the magnetic field for both directions at $T = 2.4$ K. The black line represent the a Brillouin function for spin 1/2 with appropriate g-factor of 2.5. The blue line demonstrate a Brillouin function for spin 1/2 with ferromagnetic interactions and $J = 2.4$. The pink line demonstrate a Brillouin function for spin 1/2 with ferromagnetic interactions and $J = 2.3$

with spin 1/2 and $g = 2.5$ [18]:

$$\frac{M}{\mu_B} = \frac{1}{2}g \tanh \left[\frac{\frac{1}{2}g\mu_B H}{k_B T} \right]. \quad (3.3)$$

As can be seen, the data does not fit to the Brillouin function. Brillouin function can be a good fit for high temperature measurements when interactions can be

neglected. Since our data are taken at low temperature, interactions cannot be neglected thus, Brillouin function cannot describe our data. Another thing that one should notice is that the data increase faster than the Brillouin function. Therefore, the spins feel higher magnetic field than the applied magnetic field, this could be an indication for ferromagnetic interactions.

We look at the following Hamiltonian:

$$\mathcal{H} = JS_1 \cdot S_2 + \mathbf{H} \cdot M \quad (3.4)$$

where, $M = g\mu_B S$ and \mathbf{H} is the magnetic field. Then we can write the Hamiltonian as,

$$\mathcal{H} = \frac{zJ}{g^2\mu_B^2} M_1 \cdot M_2 + M \cdot \mathbf{H} = M \left(H + \frac{zJ}{g^2\mu_B^2} M \right) = M \cdot \mathbf{H}_{eff}$$

where z is the number of neighbors and $H_{eff} = H + \frac{zJ}{g^2\mu_B^2} M$. Now we can write Brillouin function using this H_{eff} ,

$$\frac{M}{g\mu_B} = \tanh \left(\frac{\frac{1}{2}g\mu_B \mathbf{H}_{eff}}{k_B T} \right) = \tanh \left(\frac{\frac{1}{2}g\mu_B \mathbf{H} + \frac{1}{2} \frac{zJ}{g\mu_B} M}{k_B T} \right) \quad (3.5)$$

Using this equation we try to find the value of the exchange coupling J .

In Fig. 3.5 we demonstrate theoretical Brillouin functions for different values of the exchange coupling J . The blue line demonstrate a Brillouin function for spin 1/2 with ferromagnetic interactions and $J = 2.4$. The pink line demonstrate a Brillouin function for spin 1/2 with ferromagnetic interactions and $J = 2.3$. These two Brillouin functions do not fit the data. But they can indicate that there is a small difference in the interactions, perpendicular and parallel to the Kagomé plane.

3.2 ESR

ESR experiments were held at the Schulich Faculty of Chemistry, Technion. Special NMR sample tubes made of Quartz, which have no contribution to the sample signal, were used.

Using the same technique of gluing the sample's plates to a transparency slide we performed anisotropy measurements. At each direction we measured from 300 K to 15 K, the measurements were done by keeping the frequency fixed and sweeping the field. At Fig. 3.6 depicted the absorption line for the parallel and perpendicular fields at temperature of 295 K. The signal intensity at the perpendicular direction is stronger than the signal intensity of the parallel direction, which is consistent with the anisotropy SQUID measurements (Chapter 3.1). For all temperature

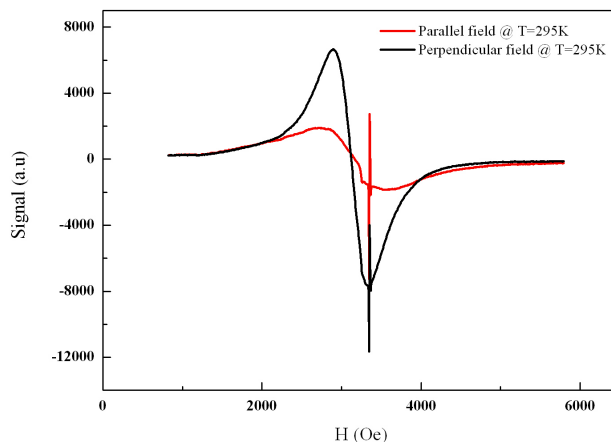


FIGURE 3.6: ESR absorption lines for the Cu(1,3-bdc) compound at 295 K for both directions, $H \parallel c$ -axis and $H \perp c$ -axis.

measurements, we integrate over the absorption signal and fitted the line with a lorentzian fit. The HWHI, δ (see Eq. 4.9), and the intensities of the signal can be extracted, from each fit. Those parameters as a function of temperature are depicted in Fig. 3.7. The g-factor at each temperature and direction was calculated by,

$$g_{\perp, \parallel} = \frac{\Delta H}{H_r} \cdot 2.0023 + 2.0023 \quad (3.6)$$

where H_r is the resonance field of the reference sample, ΔH is the difference between the resonance fields of the sample and reference and 2.0023 is the g-factor of electron in carbon-oxide which is our reference sample. Stands out from those

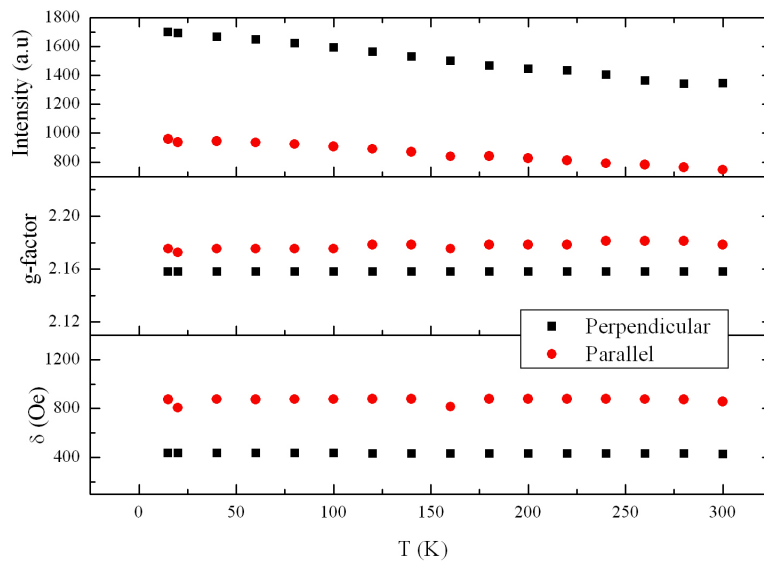


FIGURE 3.7: Temperature dependence of the linewidth, intensity and g-factor for both directions, $H \parallel c$ -axis and $H \perp c$ -axis.

graphs that the linewidths and g-factors are constant over all temperature range measured. The intensity decreases as temperature increases, an expected behavior.

3.3 μ SR

μ SR measurements were performed at the Paul Scherrer Institute (PSI), Switzerland, in the low temperature facility spectrometer with a dilution refrigerator. The measurements were carried out with the muon spin tilted at 45° relative to the beam direction. Positrons emitted from the muon decay were collected simultaneously in the forward-backward (longitudinal) and the up-down (transverse) detectors with respect to the beam direction. The powder we examine contains Cu(1,3-bdc) in the form of blue crystalline plates. However, it is mixed with some green spheres of copper-containing ligand oxidation byproduct $C_{32}H_{24}Cu_6O_{26}$ as seen in Fig. 1.5. Although we have those two different phases in our crystalline,

we manage to distinguish between the signals as we demonstrate below. In order to performed the μ SR experiment, we pressed our powder into a silver plate.

3.3.1 TF μ SR

Transverse field (TF) measurements were taken at the temperature ranging from 0.9 K to 2.8 K with a constant applied field of $H = 1$ kOe. We also performed a field calibration measurement using a blank silver plate providing the muon rotation frequency $f_s = 13.67$ MHz at the applied TF of 1 kOe.

In the inset of Fig. 3.8 we depict by symbols the muon decay asymmetry in a reference frame rotated at $H = 200$ Oe less than the TF. In the main panel of Fig. 3.8 we show the fast Fourier Transform (FFT) of the TF data at some selected temperatures. The FFT of the highest temperature, 6 K, shows a wide asymmetric peak with extra weight towards low frequencies. At 3 K the wide asymmetric peak separates into two different peaks shifting in opposite directions. At even lower temperatures the low frequencies vanishes. We assign the latter peak to to muons that stop in Cu(1,3-bdc) since such a wipe-out of the signal is typical of slowing down of spin fluctuation, which in Cu(1,3-bdc) is expected near 2 K. Previous research [10] shows a peak at the heat capacity at $T \simeq 2$ K. This special temperature may be significant at μ SR experiment and may be an indication of a change in the Cu(1,3-bdc) compound. The high frequency peak corresponds to muons that stopped at the by-product since its frequency is very close to the silver calibration. The slightly shift of the high frequency peak as the temperature is lowered is unclear.

Despite the disappearance of the low frequency peak in the frequency domain, its contribution in the time domain (inset of Fig 3.8 is clear. The high frequency peak in the main panel of Fig. 3.8 corresponds to the signal surviving for a long time in both insets of Fig. 3.8. The broad and the disappearing peak in the main panel corresponds to the fast decaying signal for the first $0.2\mu\text{sec}$ seen in the lower inset, the arrow in the inset demonstrates the frequency shift. Consequently we fit the

function

$$A_{TF}(t) = A_1 e^{\left(-\frac{R_1 t}{2}\right)} \cos(\omega_1 t + \varphi) + A_2 e^{(-R_2 t)} \cos(\omega_2 t + \varphi) + B_g \quad (3.7)$$

to our data in the time domain globally, where the parameters R_1 and ω_1 are the relaxation and angular frequency of the byproduct, and R_2 and ω_2 are the relaxation and angular frequency of the Kagomé part. The parameters $A_1 = 0.0049(4)$, $A_2 = 0.125(3)$, $R_1 = 0.13(1)(\mu\text{sec}^{-1})$, φ and B_g are shared in the fit, while R_2, ω_1, ω_2 are free. The quality of the fit is represented in the inset of Fig. 3.8 by the solid lines. The ratio of A_1 to A_2 supports the assignment of the fast relaxing signal to Cu(1,3-bdc).

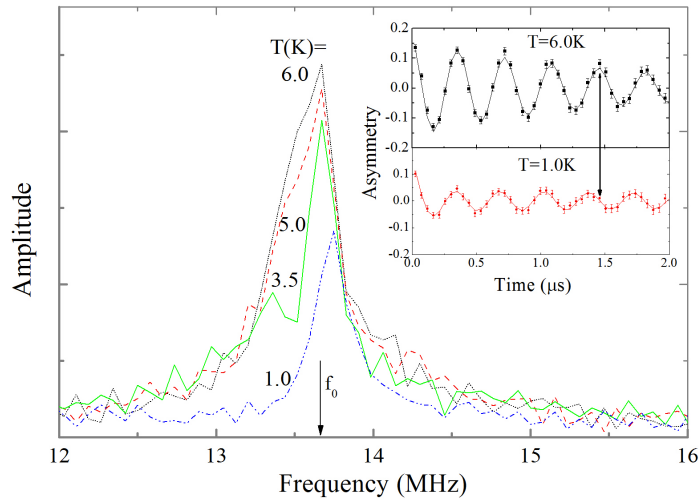


FIGURE 3.8: FFT of the asymmetry data in a field of 1 kOe transverse to the initial muon spin direction. f_0 is the reference frequency in pure silver. Inset: transverse field asymmetry in the time domain and rotating reference frame

In Fig. 3.9 we plot the shift, $K_{1,2} = \frac{\omega_s - \omega_{1,2}}{\omega_s}$, versus temperature, where $\omega_s = 2\pi f_s$. As expected K_2 increases with decreasing temperatures. The small decrease of K_1 is not expected and is not clear to us at the moment.

The muon transverse relaxation, R_2 , is also presented in Fig. 3.9. It has roughly the same temperature behavior as the shift, K_2 . However, at $T = 1.8$ K, R_2 seems to flatten out before increasing again around 1 K. This is somewhat surprising.

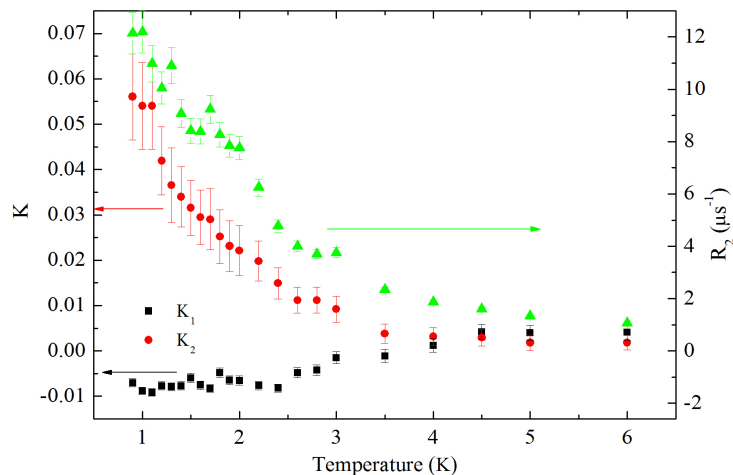


FIGURE 3.9: K_1 , black squares, is the Muon shift from muons that stopped at $C_{32}H_{24}Cu_6O_{26}$ (the non-magnetic by product) and K_2 , red spots, the muon shift from muons that stopped at Cu(1,3-bdc) depicted versus temperature. R_2 , green triangles, the relaxation rate from Cu(1,3-bdc) depicted versus temperature.

In Fig. 3.10(a) we depict the macroscopic magnetization M measured with a superconducting quantum interference device magnetometer versus K_2 . The magnetization is also measured at 1 kOe. The plot indicates that in the temperature range where both M and K_2 are available they are proportional to each other. Therefore, $\sum_k \bar{A}_k$ is temperature independent. As described in the experimental methods chapter, we expect $R_2 \propto K_2$ if the σ_k (see Eq. 2.11) are temperature-independent parameters. A plot of R_2 versus K_2 , shown in Fig. 3.10(b), indicates that R_2 is not proportional to or even does not depend linearly on K_2 and a kink is observed at $T_0 = 1.8$ K. This result suggests a change in the hyperfine field distribution at T_0 . An interesting possible explanation for such a change is a response of the lattice to the magnetic interactions via a magnetoelastic coupling [19, 20].

However, unlike a similar situation in a pyrochlore lattice [21], it seems that here the lattice is becoming more ordered upon cooling since the rate of growth of R_2 below T_0 is lower than at higher temperatures.

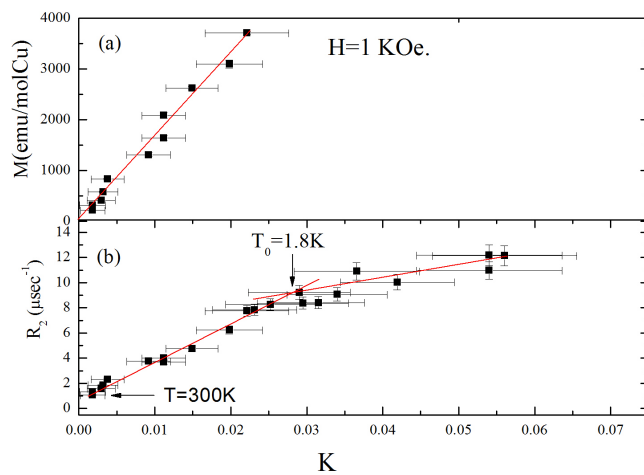


FIGURE 3.10: (a) Magnetization versus the muon shift in Cu(1,3-bdc). (b) The muon relaxation versus the muon shift in Cu(1,3-bdc).

3.3.2 LF μ SR

The longitudinal-field (LF) measurements were taken at several different fields between 50 Oe and 3.2 kOe with a constant temperature of 0.9 K. The zero-field measurements were taken in the longitudinal configuration at a temperature ranging from 0.9 K to 2.8 K.

The μ SR LF data including ZF are presented in Fig. 3.11. The LF data at the lowest temperature of 0.9 K are depicted in panel (a). At this temperature and a field of 50 Oe, the muon asymmetry shows a minimum at around $0.1\mu\text{sec}$. At longer times the asymmetry recovers. The ZF data at three different temperatures are shown in Fig. 3.11(b). The relaxation rate increases as temperature decreases due to slowing down of spin fluctuations, until at the lowest temperature the dip appears. We saw no difference in the raw data between 1.0 K and 0.9 K and therefore did not cool any further. Both LF and ZF data fit the theory expected. These are unusual μ SR data in a Kagomé magnet, in the sense that spin fluctuations are slow enough compared to the internal field scale to expose the static nature of the muon spin relaxation function, namely, the dip, and to allow calibration of the internal field distribution. Other Kagomé magnets show the same general behavior but without this dip [22–24].

The experimental asymmetry is fitted with $A_{LF} = A_0 \bar{P}_z(\nu, H, \Delta, t) + B_g$.

$\bar{P}_z(\nu, H, \Delta, t)$ is the Dynamic Gaussian Kubo-Toyabe. The relaxation from the second green phase is very small and is absorbed in the background factor B_g . In the fit of the field-dependence experiment at the lowest temperature, presented in Fig. 3.11(a) by the solid lines, Δ, ν, A_0 and B_g are shared parameters. We found $\Delta = 19.8(4)$ MHz and $\nu = 3.6(2)\mu\text{sec}^{-1}$.

This indicates that the spins are not completely frozen even at the lowest temperature [25].

When analyzing the ZF data at a variety of temperatures, shown in Fig. 3.11(b) by the solid lines, we permit only ν to vary. The fit is good at the low temperatures but does not capture the 2.8 K data at early times accurately. However, the discrepancy is not big enough to justify adding more fit parameters. We plot the the temperature dependence of the fluctuation rate in Fig. 3.12.

ν hardly changes while the temperature decreases from $T = 2.8$ K down to $T_0 = 1.8$ K. From T_0 , ν decreases with decreasing temperatures, but saturates below 1 K. This type of behavior was observed in a variety of frustrated Kagomé [22–24] and pyrochlore [26, 27] lattices. It is somewhat different from classical numerical simulation where ν decreases with no saturation [28, 29]. In fact, the numerical ν is a linear function of the temperature over three orders of magnitude in T [29].

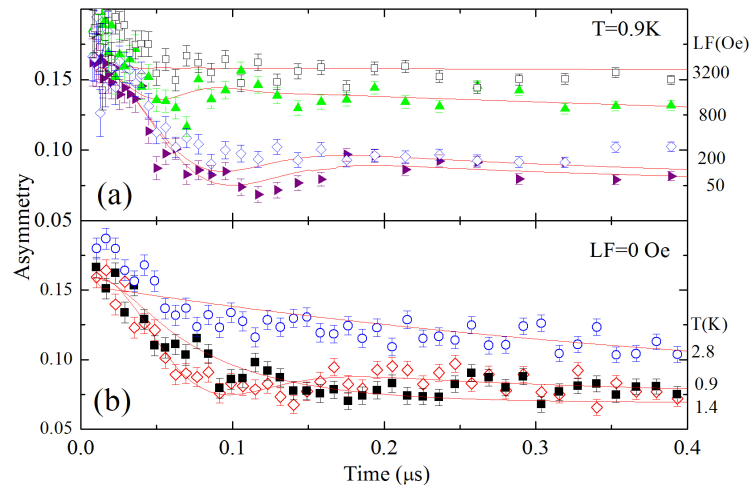


FIGURE 3.11: (a) The asymmetry at various longitudinal fields and $T = 0.9$ K. (b) The asymmetry at zero field for various temperatures.

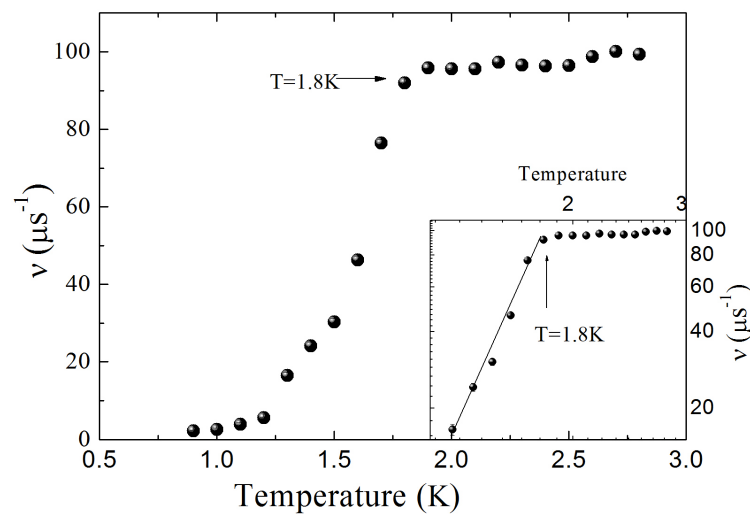


FIGURE 3.12: The fluctuation rate ν versus temperature. Inset: ν near 1.8 K on a log-log scale. (The error bars are smaller than the symbol size)

Chapter 4

Discussion

In this chapter we will discuss the experimental results and try to connect between theory and experiment.

4.1 Susceptibility in an anisotropic spin Hamiltonian

Magnetization measurements reveal anisotropy susceptibility. Therefore we would like to examine how anisotropic spin Hamiltonian including the Dzyaloshinsky Moriya interactions (DMI) influence the susceptibility. The Hamiltonian which we consider is:

$$\mathcal{H} = \sum_{i < j} \left(J_{ij} \vec{S}_i \cdot \vec{S}_j + D_{ij} S_i^z \cdot S_j^z + D_{ij} (S_j \times S_i) + g\mu_B S_i \cdot \mathbf{H} \right) \quad (4.1)$$

where \mathcal{D}_{ij} is the Dzyaloshinsky Moriya vector and D_{ij} is Ising anisotropy. By using the vector relation, $A \cdot (B \times C) = B \cdot (C \times A)$, the Hamiltonian can be written as,

$$\mathcal{H} = \frac{1}{2} \sum_i S_i \cdot \left(\sum_{j \neq i} \tilde{J}_{ij} S_j + \mathcal{D}_{ij} \times S_j + g\mu_B \mathbf{H} \right) \quad (4.2)$$

where,

$$\tilde{J}_{ij} = \begin{pmatrix} J_{\perp} & 0 & 0 \\ 0 & J_{\perp} & 0 \\ 0 & 0 & J_z \end{pmatrix}$$

and $J_z = J + D$, $J_{\perp} = J_x = J_y = J$. This Hamiltonian can be written as $\mathcal{H} = g\mu_B \sum_i S_i \cdot \mathcal{H}_{eff}$, where the effective field,

$$\mathcal{H}_{eff} = \frac{1}{2} \frac{1}{g\mu_B} \sum_j \left(\tilde{J}S_j + \mathcal{D}_{ij} \times S_j \right) + \mathbf{H}$$

The mean field approximation means $S_j \longrightarrow \frac{M}{g\mu_B}$ thus,

$$\mathcal{H}_{eff} = \frac{1}{2} \frac{Z}{(g\mu_B)^2} \left(\tilde{J}M + D \times M \right) + \mathbf{H} \quad (4.3)$$

where $\mathcal{D} = \frac{1}{Z} \sum_j \mathcal{D}_{ij}$, and Z is the number of near neighbors.

Therefore the magnetization is given by,

$$M = \frac{C}{T} \left(\frac{1}{2} \frac{Z}{(g\mu_B)^2} \left(\tilde{J}M + \mathcal{D} \times M \right) + H \right) \quad (4.4)$$

C is the Curie constant, $C = \frac{Ng^2\mu_B^2 S(S+1)}{3k_B}$ where N is the number of atoms in a unit cell, g is the g-factor and S the spin number. Since we are interested in the magnetization we get,

$$\mathbf{M} = C \left(T\mathbf{I} - \tilde{\theta}_{cw} - \mathbf{A} \right)^{-1} \mathbf{H} \quad (4.5)$$

$$\tilde{\theta}_{cw} = \frac{1}{2} \frac{CZ}{(g\mu_B)^2} \begin{pmatrix} J_{\perp} & 0 & 0 \\ 0 & J_{\perp} & 0 \\ 0 & 0 & J_z \end{pmatrix}$$

$$\theta_{z,\perp} = \frac{1}{2} \frac{ZS(S+1)J}{3k_B}$$

$$\mathbf{A} = \frac{CZ}{(g\mu_B)^2} \begin{pmatrix} 0 & -\mathcal{D}_z & \mathcal{D}_y \\ \mathcal{D}_z & 0 & -\mathcal{D}_x \\ -\mathcal{D}_y & \mathcal{D}_x & 0 \end{pmatrix}$$

Another form to write Eq. 4.5 is by defining

$$B = \begin{pmatrix} T - \theta_\perp & \mathcal{D}'_z & -\mathcal{D}'_y \\ -\mathcal{D}'_z & T - \theta_\perp & \mathcal{D}'_x \\ \mathcal{D}'_y & -\mathcal{D}'_x & T - \theta_z \end{pmatrix}$$

and

$$\mathcal{D}' = \frac{CZ}{(g\mu_B)^2} \mathcal{D}$$

then getting,

$$\mathbf{M} = C\mathbf{B}^{-1}\mathbf{H}$$

Now, we can calculate $B_{3,3}^{-1} = B_z^{-1}$,

$$B_{3,3}^{-1} = C \frac{(T - \theta_\perp)^2 + \mathcal{D}'_z{}^2}{(T - \theta_z)(T - \theta_\perp)^2 + T\vec{\mathcal{D}}'^2 - \mathcal{D}'_\perp{}^2\theta_\perp - \mathcal{D}'_z{}^2\theta_z}$$

In the high temperature regime,

$$\lim_{T \rightarrow \infty} B_{3,3}^{-1} = \frac{1}{(T - \theta_z)} \quad (4.6)$$

$B_{1,1}^{-1} = B_x^{-1}$ can also calculate,

$$B_{1,1}^{-1} = C \frac{(T - \theta_\perp)(T - \theta_z) + \mathcal{D}'_x{}^2}{(T - \theta_z)(T - \theta_\perp)^2 + T\vec{\mathcal{D}}'^2 - \mathcal{D}'_\perp{}^2\theta_\perp - \mathcal{D}'_z{}^2\theta_z}$$

Again, let's look at the high temperature regime,

$$\lim_{T \rightarrow \infty} B_{1,1}^{-1} = \frac{1}{(T - \theta_\perp)} \quad (4.7)$$

From the calculation above we conclude that, \mathcal{D} , Dzyaloshinsky Moriya interactions does not contribute to Curie-Weiss temperature in the z or the perpendicular

directions. In general, the susceptibility, $\chi = \frac{M}{H}$, gets the form,

$$\chi = C \frac{(T - \theta_{\perp})^{1+\rho} (T - \theta_z)^{1-\rho} + \rho \mathcal{D}'_z{}^2 + (1 - \rho) \mathcal{D}'_x{}^2}{(T - \theta_z) (T - \theta_{\perp})^2 + T \vec{\mathcal{D}}'^2 - D'_{\perp}{}^2 \theta_{\perp} - \mathcal{D}'_z{}^2 \theta_z} \quad (4.8)$$

using $\rho = 1$ for χ_z and $\rho = 0$ for χ_x .

Since DMI is not contributing to θ_{CW} another term must be added to the Hamiltonian. Before we look directly at the Hamiltonian we will introduce the method of moments.

4.2 ESR linewidth in terms of moments

The ESR line-shape is a resonance curve which can be described by a Gaussian or a Lorentzian curve. Our data is best fitted to a Lorentzian curve hence we will not consider the Gaussian curve in this discussion. The Lorentzian normalized function is described by the function,

$$\frac{\chi''(H, \omega)}{H} = \frac{1}{\pi} \frac{\gamma \delta}{(\gamma \delta)^2 - (H - H_0)} \quad (4.9)$$

We assume,

$$\frac{\chi''(H, \omega)}{\omega} = \frac{1}{\pi} \frac{\delta}{\delta^2 - (\omega - \omega_0)} \quad (4.10)$$

where δ is the Half Width Half Intensity (HWHI) and ω_0 is the absorption frequency. $f(\omega)$ has maximum at ω_0 . The n th moment for a resonance curve defined by

$$M_n = \int (\omega - \omega_0)^n f(\omega) d\omega$$

To calculate the second and forth moments of a Lorentzian a cut-off must be used since they diverge. One model which can be used is describing Eq. 4.9 within the

interval $|\omega - \omega_0| \leq \alpha$ with $\alpha \gg \delta$ and zero outside the interval thus we get [30],

$$M_2 = \frac{2\alpha\delta}{\pi}, \quad M_4 = \frac{2\alpha^3\delta}{3\pi} \quad (4.11)$$

Hence we find that,

$$\delta = \Delta\nu_{1/2} = \frac{\pi}{2\sqrt{3}} M_2 \sqrt{\frac{M_2}{M_4}} \quad (4.12)$$

$\Delta\nu_{1/2}$ is the HWHI and M_2 and M_4 are the second and 4th moment of a resonance curve. The linewidth turns out to be independent of the cut-off α .

Using the method of moments [30] we will show the connection between the imaginary susceptibility (Eq. 4.14) and M_2 , M_4 . The total Hamiltonian is

$$\mathcal{H} = \mathcal{H}_0 + \mathcal{H}_1$$

where \mathcal{H}_0 is the Zeeman Hamiltonian

$$\mathcal{H}_0 = g\mu_B H \sum_j S_z^j \quad (4.13)$$

and \mathcal{H}_1 is a perturbing Hamiltonian. The resonance line shape is symmetric with respect to the central frequency ω_0 , to each transition at frequency $\omega_0 + u$ corresponds an equal intensity transition at $\omega_0 - u$. If $f(\omega)$ is the symmetric normalized shape function, $h(u) = f(\omega_0 + u)$ is an even function of u .

The resonance curve is described by χ'' , as explained earlier, in Chapter 2.

In terms of the electronic spins $\chi''(H, \omega)$ is given by,

$$\chi''_{\alpha\beta}(H, \omega) = \frac{(g\mu_B)^2}{2\hbar V} \frac{\hbar\omega}{K_B T} \int_{-\infty}^{\infty} \langle \{S_\alpha^I(t), S_\beta^I(0)\} \rangle \exp(i\omega t) dt \quad (4.14)$$

where

$$S_\alpha^I(t) = \exp\left(\frac{i\mathcal{H}t}{\hbar}\right) S_\alpha \exp\left(-\frac{i\mathcal{H}t}{\hbar}\right) \quad (4.15)$$

where \mathcal{H} is the Hamiltonian. Thus for the moments calculation we will use Eq. 4.14. we define $G(t) = \langle \{S_\alpha^I(t), S_\beta^I(0)\} \rangle$. Previously we described the time evaluation of the spin operator by Eq. 4.15. Using $\mathcal{H} = \mathcal{H}_0 + \mathcal{H}_1$ and the fact that Zeeman Hamiltonian only determined the position of the line and not the shape of the line, hence the shape of the line is determined by the relaxation function

$$G_1(t) = \left\langle \left\{ \exp\left(\frac{i\mathcal{H}_1 t}{\hbar}\right) S_x \exp\left(-\frac{i\mathcal{H}_1 t}{\hbar}\right), S_x \right\} \right\rangle \quad (4.16)$$

Using the inverse Fourier transform of Eq. 4.14, $G_1(t)$ up to a temperature dependent normalization factor can be written as,

$$G_1(t) = \frac{1}{2\pi\xi} \int_{-\infty}^{\infty} \frac{\chi''(0, \omega)}{\omega} e^{-i\omega t} d\omega. \quad (4.17)$$

where $\xi = \frac{(g\mu_B)^2}{2\hbar V} \frac{\hbar}{K_B T}$ and the moments of a curve are given by,

$$M_n = \int_{-\infty}^{\infty} \frac{\chi''(0, \omega)}{\omega} \omega^n d\omega$$

where $\frac{\chi''(0, \omega)}{\omega}$ is an even function of ω . The odd moments vanish and the even moments are given by

$$M_{2n} = \frac{(-1)^n \left(\frac{d^{2n} G_1(t)}{dt^{2n}} \right)_{t=0}}{G_1(0)} \quad (4.18)$$

From the definition of $G_1(t)$ 4.16 we find that the value of its n th derivative for $t = 0$ is

$$\left(\frac{d^n G_1(t)}{dt^n} \right)_{t=0} = (i)^n \{ [\mathcal{H}_1, [\mathcal{H}_1, [\dots, [\mathcal{H}_1, S_x] \dots]]], S_x \} \quad (4.19)$$

Finally, From Eq. 4.19 and 4.18 we obtain the second and forth moments,

$$M_2 = - \frac{Tr([\mathcal{H}_1, S_x]^2)}{Tr(S_x^2)} \quad (4.20)$$

$$M_4 = \frac{\text{Tr}([\mathcal{H}_1, [\mathcal{H}_1, S_x]]^2)}{\text{Tr}(S_x^2)} \quad (4.21)$$

In order to calculate the second and fourth moments obtained in Eq. 4.20 and Eq. 4.21 we must define our spin Hamiltonian.

We consider a fully anisotropy Hamiltonian, not including the DMI,

$$\mathcal{H} = \sum_{j < k} \left[J_{jk} \vec{S}_j \cdot \vec{S}_k + D_{jk} S_{jz} S_{kz} + E_{jk} (S_{jx} S_{kx} - S_{jy} S_{ky}) \right] \quad (4.22)$$

where J_{ij} is the exchange anisotropy coupling coefficient and D_{ij}, E_{ij} are the spin-orbit coupling coefficients for the z direction and the $x - y$ plane respectively (as mentioned before, the kagomé planes are at the $x - y$ plane). We analyze the Hamiltonian just with J, E and D to see if we can understand the compound with these three interactions only.

After calculating the theoretical moments for a lattice given, the calculated linewidth can be compared to the experimental linewidth. This comparison additionally to $\theta_{cw}^z = J + D$ (explained in 4.1), taken from magnetization measurements, yields the Hamiltonian parameters J, D, E .

Before we start with the calculations, let us go through the notations. We shall suppose that the constant magnetic field H is applied in the z direction, and that the oscillating field whose absorption is being studied is along the x axis. In that case, we will calculate M_2^{\parallel} and M_4^{\parallel} . When the applied magnetic field is in the x direction we will calculate M_2^{\perp} and M_4^{\perp} . All following calculations are done for spin $1/2$ and nearest neighbors interaction.

To practice the method of moments, we start by looking at a 1D spin chain (Fig. 4.1). Now, we can calculate the second and fourth moments for the chain using Eq. 4.20 and Eq. 4.21.

The scalar product $\vec{S}_i \cdot \vec{S}_j$ will not contribute, to the second moment calculation, since $\left[\sum_{j < k} J_{jk} \vec{S}_i \cdot \vec{S}_j, S_x \right] = 0$.

The contribution of the symmetric anisotropy exchange to the commutator takes



FIGURE 4.1: One dimensional spins chain.

the form,

$$\left[\sum_{j < k} D_{jk} S_{jz} S_{kz} + E_{jk} (S_{jx} S_{kx} - S_{jy} S_{ky}), S_x \right] = \quad (4.23)$$

$$i \sum_{j < k} (D_{jk} + E_{jk}) (S_{jy} S_{kz} + S_{jz} S_{ky}).$$

Using the relations,

$$\begin{aligned} Tr(S_\alpha)^2 &= \frac{1}{2} 2^{N-1} & \alpha = x, y, z \\ Tr(S_\alpha S_\beta)^2 &= \frac{1}{8} 2^{N-1} & \alpha, \beta = x, y, z \\ Tr(S_\alpha S_\beta S_\gamma)^2 &= \frac{1}{32} 2^{N-1} & \alpha, \beta, \gamma = x, y, z \end{aligned} \quad (4.24)$$

Finally we get for the second moment,

$$M_2^{\parallel} = (D + E)^2$$

and

$$M_2^{\perp} = 4E^2.$$

Despite the fact that the exchange coupling, J_{jk} , does not contribute to the second moment, it greatly increases the fourth moment.

For spin 1/2 nearest neighbors interaction we get:

$$M_4^{\perp} = E^2 \left[\frac{3}{2} J^2 + 3E^2 + \frac{1}{2} D^2 + JD \right]$$

$$M_4^{\parallel} = \frac{(E + D)^2}{4} \left[\frac{3}{2} J^2 + \frac{3}{2} E^2 + D^2 + JD + ED \right]$$

Hence the linewidth, using Eq. 4.12, for each direction is,

$$\delta^{\parallel} = \frac{\pi}{\sqrt{3}} (D + E)^2 \sqrt{\frac{1}{\left[\frac{3}{2} J^2 + \frac{3}{2} E^2 + D^2 + JD + ED \right]}} \quad (4.25)$$

$$\delta^{\perp} = \frac{\pi}{\sqrt{3}} E^2 \sqrt{\frac{1}{\left[\frac{3}{2} J^2 + 3E^2 + \frac{1}{2} D^2 + JD \right]}} \quad (4.26)$$

For example, the case where $D, E \ll J$ yields,

$$\delta^{\parallel} = \frac{\pi\sqrt{2}}{3} \frac{(D + E)^2}{J}, \quad \delta^{\perp} = \frac{\pi\sqrt{2}}{3} \frac{E^2}{J}$$

i.e. the exchange coupling, J , narrows the ESR lines. The spin-orbit coupling, E , affects ESR lines in both directions of measurements, but the spin-orbit coupling in the z direction does not contribute the perpendicular linewidth. After doing the calculation for 1D spins chain let's look at a single triangle. We have to write the interactions by taking projections of the spins onto vectors parallel and perpendicular to the bond. The bonds shown in Fig. 4.2 are defined by:

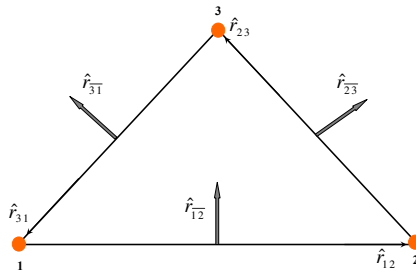


FIGURE 4.2: Two dimensional triangle bonds.

$$\begin{aligned} r_{12} &= \hat{x} ; r_{\overline{12}} = \hat{y} \\ r_{23} &= (-\cos 60^\circ, \sin 60^\circ) ; r_{\overline{23}} = (\cos 30^\circ, \sin 30^\circ) \\ r_{13} &= (-\cos 60^\circ, -\sin 60^\circ) ; r_{\overline{31}} = (-\cos 30^\circ, \sin 30^\circ) \end{aligned} \quad (4.27)$$

The Hamiltonian described by Eq. 4.22 becomes slightly more difficult.

$$\begin{aligned}
\mathcal{H}_{triangle} = & \sum_{i<j} \left[J_{ij} \vec{S}_i \cdot \vec{S}_j + D_{ij} S_{iz} S_{jz} \right] \\
& + \frac{1}{2} E \left(2S_x^1 S_x^2 - 2S_y^1 S_y^2 - S_x^2 S_x^3 + S_y^2 S_y^3 - S_x^3 S_x^1 - S_y^3 S_y^1 \right) \\
& - \frac{\sqrt{3}}{2} E \left(S_x^2 S_y^3 - S_y^2 S_x^3 - S_x^3 S_y^1 + S_y^3 S_x^1 \right)
\end{aligned} \tag{4.28}$$

The third term of this Hamiltonian will add non-diagonal elements. Those elements have the form $S_x^j S_y^k$. They mix the x, y directions. This contribution increases the difficulty of the fourth moment calculation, thus the calculation of the linewidths become more complicated.

To complete the all picture we would like to look at a kagomé lattice [see Fig.1.3. The moments calculation for the kagomé lattice combine both the spins chain and the triangle case. The fourth moment, especially, represent a very tedious calculation involving a large number of terms. The calculation was done by Dr. Ravi Chandra and Dr. Daniel Podolsky.

$$M_2^\perp = 16E^2 \tag{4.29}$$

$$M_2^\parallel = 4(E^2 + D^2) \tag{4.30}$$

and

$$M_4^\perp = 2E^2 (4D^2 + 9DJ + 8(E^2 + J^2)) \tag{4.31}$$

$$\begin{aligned}
M_4^\parallel = & \frac{7D^4}{4} + 2D^3 J - DE^2 J + \\
& D^2 (4E^2 + 3J^2) + \frac{1}{2} E^2 (5E^2 + 9J^2)
\end{aligned} \tag{4.32}$$

4.2.1 Hamiltonian parameters

In order to calculate the Hamiltonian parameters, J , D and E we have to solve the three following equations: The first equation was already presented, Eq. 3.2 which is

$$-\theta_{CW}^{\parallel} = J + D = -4.03 \text{ K} \cdot 2 = -8.06 \text{ K}$$

and two other which connect theory to experiment,

$$\frac{2\pi f}{20.048} \cdot \frac{\delta_{\parallel}}{H_{\parallel}} = \frac{\pi}{2\sqrt{3}} M_2^{\parallel} \cdot \sqrt{\frac{M_2^{\parallel}}{M_4^{\parallel}}} \quad (4.33)$$

$$\frac{2\pi f}{20.048} \cdot \frac{\delta_{\perp}}{H_{\perp}} = \frac{\pi}{2\sqrt{3}} M_2^{\perp} \cdot \sqrt{\frac{M_2^{\perp}}{M_4^{\perp}}} \quad (4.34)$$

The numerical solutions of these three equations are: According the chosen Hamil-

J[K]	D[K]	E[K]
-9.273	1.213	± 0.477
-6.975	-1.085	± 0.449

TABLE 4.1: Numerical solutions for the spin Hamiltonian parameters.

tonian, $J + E$ and $J - E$ must be positive in order to get AFM interactions. All the solutions gives FM interactions. There can be several hypothesis for this outcome. One consideration could be the cut-off selection in the ESR experiment, which affects the moments calculations. Maybe the selection of the cut-off was wrong, but in order to get AFM interactions a we need to make a robust change in the cut-off selection. Another possibility can be related to our Hamiltonian. We considered the simplest anisotropy Hamiltonian with n.n. interactions. Maybe more general Hamiltonian should be taken into account. Hamiltonian with n.n.n interactions and even DMI should be considered. The last and interesting option is that the cut-off selection is correct and the Hamiltonian describes well our system. In this case we can say that we found new state of matter. Kagomé with ferromagnetic interactions with no long-range order and a dynamic ground state.

4.3 μ SR result against theory

J. Robert *et al.* [29] investigate the classical spin dynamics of the Kagomé AFM by combining Monte Carlo and spin dynamic simulation. Their numerical simulation show slowing down of spin fluctuation but no spin freezing even at the lowest temperature Fig. 4.3(a). The numerical relaxation, Γ_a compared with ν , spin relaxation rate, exhibit a linear function of the temperature, over three orders of magnitude.

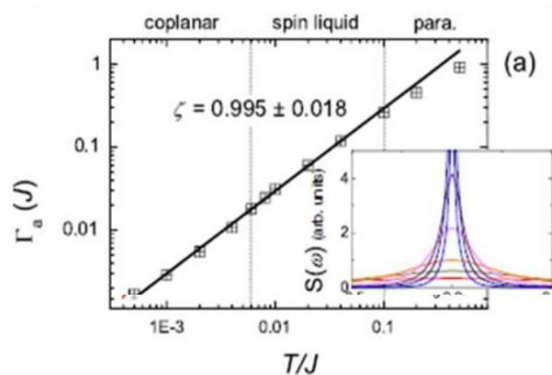


FIGURE 4.3: The numerical relaxation, Γ_a compared with ν exhibit a linear function of the temperature.

The inset of Fig. 3.12 shows the fluctuation rate, ν , as a function of temperature near T_0 on a log-log scale where slowing down begins. Only near T_0 our data are consistent with a linear relation

$$\nu - \nu_\infty = \nu_0 (T - T_0),$$

where ν_∞ is the high temperature fluctuation rate.

The discrepancy with the numerical work [29] might be because μ SR probes field correlation involving several spins nearing the muon, while the simulations concentrate on spin-spin auto correlations (with a decay Γ_a compared here with ν). At our lowest temperature the rotations of ensemble of spins are already coherent therefore field and spin correlations are not identical. Another possibility is that

the saturation of ν with decreasing T is a pure quantum effect not captured by the classical simulations.

Chapter 5

Conclusions

In this work we characterize the Hamiltonian and investigate the ground state of the new Kagomé lattice, Cu(1,3-bdc). We found that the susceptibility of this system is not isotropic, and in particular the Curie-Weiss temperature differs between different measurement directions.

We demonstrated that DMI does not influence the Curie-Weiss temperature suggesting that the exchange interaction are responsible for the anisotropy.

Electron Spin Resonance experiment combined with the anisotropic exchange assumption allowed us to determine the spin Hamiltonian parameters. The method of moments for determining the exchange parameters gives ferromagnetic interactions in all directions.

The characterization of Cu(1,3-bdc) ground state was done with μ SR. It shows that Cu(1,3-bdc) has a special temperature $T_0 = 1.8$ K. The susceptibility, measured by the μ SR frequency shift, grows monotonically upon cooling even past this temperature. In contrast, the muon spin line-width, which also grows upon cooling, halts around 1.8 K. This might be explained by a subtle structural transition.

The most important finding of μ SR is the absence of long range order and slow spin fluctuations in the limit of zero temperature. These finding are typical to system with strong frustration. However, the μ SR result are surprising in light of

the presence of ferromagnetic interaction found by ESR; A ferromagnetic Kagomé is not frustrated and should freeze. Whether we found a new state of matter, or have a problem with either experiments or interpretations remain to be seen.

Bibliography

- [1] X. Obradors, A. Labarta, A. Isalgu, and J. Tejada. *Solid State Commun.*, 5 (189), 1988.
- [2] A. Keren, K. Kojima, L.P. Le, G.M. Luke, W.D. Wu, and Y.J. Uemura. *Phys. Rev. B*, 53(10), 1996.
- [3] Z. Horoi, M. Hanawa, N. Kobayashi, M. Nohara, H. Takagai, Y. Kato, and M. Takigawa. *J. Phys. Soc. Jpn.*, 70(3377), 2001.
- [4] Y. Okamoto, H. Yoshida, and Z. Horoi. *J. Phys. Soc. Jpn.*, 78(033701), 2009.
- [5] R.H. Colman, C. Ritter, and A.S. Wills. *Chemistry of Materials*, 20(25), 2008.
- [6] O. Jason, J. Richter, and H. Rosner. *Journal of Physics: Conference Series*, 145(012008), 2009.
- [7] F. Bert, S. Nakamae, F. Ladieu, D. L'Hote, P. Bonville, F. Duc, J.-C. Trombe, and P. Mendels. *Phys. Rev. B.*, 76(132411), 2007.
- [8] A. Olariu, P. Mendels, F. Bert, F. Duc, J.-C. Trombe, M.A. de Vries, and A. Harrison. *Phys. Rev. Lett.*, 100(087202), 2008.
- [9] M.A. de Vries, K.V. Kamenev, J. Sanchez-Benitez, and A. Harrison. *Phys. Rev. Lett.*, 100(157205), 2008.
- [10] E. A. Nytko, J. S. Helton, P. Müller, and D. G. Nocera. *J. Am. Chem. Soc.*, 130(2922), 2008.

-
- [11] R.S. Alger. *Electron Paramagnetic Resonance: Techniques and Applications*, 1968.
- [12] C.P. Poole. *Electron Paramagnetic Resonance: A Comprehensive Treatise on Experimental Techniques*, Courier Dover Publications, 1996.
- [13] P. Carretta and A. Keren. *arXiv.*, 0905.44144, 2009.
- [14] R. S. Hayano, Y. J. Uemura, J. Imazato, N. Nishida, T. Yamazaki, and R. Kubo. *Phys. Rev. B.*, 20(850), 1979.
- [15] A. Keren. *Journal of Physics: Condensed Matter*, 16, 2004.
- [16] W.H. Press, B.p. Flannery, A.A. Teukolsky, and W.T. Vetterling. *Numerical recipes*(Cambridge University Press, Cambridge, 1989.
- [17] Emily A. Nytko. *Thesis*, 2009.
- [18] N. David Mermin Neil W. Ashcroft. Solid State Physics.
- [19] A. Keren and J.S. Gardner. *Phys. Rev. Lett.*, 87(177201), 2001.
- [20] F. Wang and A.Vishwanath. *Phys. Rev. Lett.*, 100(077201), 2008.
- [21] E. Sagi, O. Ofer, A. Keren, and J.S. Gardner. *Phys. Rev. Lett.*, 94(237202), 2005.
- [22] A. Keren, Y.J. Uemura, G. Luke, P. Memdels, M. Mekata, and T. Asano. *Phys. Rev. Lett.*, 84(3450), 2000.
- [23] A. Fukayata, Y. Fudamoto, I.M. Gat, T. Ito, M.I. Larkin, M.T. Savici, Y.J. Uemura, P.P. Kyriakou, G.M. Luke, M.T. Rovers, K.M. Kojima, A. Keren, M. Hanawa, and Z. Hiroi. *Phys. Rev. Lett.*, 91(207603), 2003.
- [24] D. Bono, P. Mendels, G. Collin, N. Blanchard, F. Bert, A. Amato, C. Baines, and A.D. Hiller. *Phys. Rev. Lett.*, 93(187201), 2004.
- [25] L. Marcipar, O. Ofer, A. Keren, E.A. Nytko, D.G. Nocera, Y.S. Lee, J.S. Helton, and C. Baines. *Phys. Rev. B.*, 80(132402), 2009.

-
- [26] S.R. Dunsinger, R.F Kiefl, K.H. Chow, B.D. Gaulin, M.J.P. Gingras, J.E. Greedan, A. Keren, K. Kojima, G.M. Luke, W.A. MacFarlane, N.P. Raju, J.E. Sonier, Y.J. Uemura, and W.D. Wu. *Phys. Rev. B.*, 54(9019), 1996.
- [27] P. Dalmas de Réotier, A. Yaouanc, L. Keller, A. Carvellino, B. Roessli, C. Baines, A. Forget, C. Vaju, P.C.M. Gubbens, A. Amato, and P.J.C. king. *Phys. Rev. Lett.*, 96(127202), 2006.
- [28] A. Keren. *Phys. Rev. Lett.*, 72(3254), 1994.
- [29] B. Canals, V. simonet, J. Roberts, and R. Ballou. *Phys. Rev. Lett.*, 101(117207), 2008.
- [30] A. Abragam. *The Principles of Nuclear Magnetism*, Oxford, 1961.

**מצב היסוד וערעורים של שריג
קגומה בעל ספין $1/2$**

ליטל מרסיפר גולדשטיין

מצב היסוד וערעורים של שריג קגומה בעל ספין $1/2$

חיבור על מחקר

לשם מילוי חלקי של הדרישות לקבלת התואר
מגיסטר למדעים בפיזיקה

ליטל מרסיפר גולדשטיין

הוגש לסנט הטכניון – מכון טכנולוגי לישראל

אוקטובר 2010

חיפה

תשרי תשע"א

חיבור על מחקר נעשה בהנחיית פרופ' עמית קרן

בפקולטה לפיסיקה

הכרת תודה

הנני אסירת תודה לפרופ' עמית קרן על ההזדמנות שניתנה לי להשתלב במחקר המרתק, על ההנחיה המעולה ועל כל העזרה והתמיכה.

אני מודה לכל חברי הקבוצה על העזרה ועל התקופה שעברנו יחד.

אני מודה לדר' רבי צ'נדרה ודר' דניאל פודולסקי על העזרה בחישובים תיאורטיים.

אני מודה לדר' אהרון בלנק ודר' בוריס טומנסקי, מהפקולטה לכימיה, על העזרה בניסויי תהודה מגנטית אלקטרונית.

אני מודה למשפחתי על העזרה, התמיכה והעידוד האינסופי לאורך כל תקופת לימודיי.

תודה מיוחדת לבעלי מנחם, על אהבתו ותמיכתו האינסופית.

אני מודה לטכניון על התמיכה הכספית הנדיבה במהלך השתלמותי

תקציר

מרבית החומרים המגנטיים, בטמפרטורות גבוהות, הינם פאראמגנטיים כלומר, המומנטים המגנטיים (הספינים) נמצאים בתסיסה תרמית ורנדומיים במיקומם. בטמפרטורות נמוכות, אינטרקציות ספין-ספין הופכות למשמעותיות יותר ומשפיעות על סידור הספינים בגביש על מנת למזער את האנרגיה, בהתאם לחוקי התרמודינמיקה. בחומרים אנטי-פרומגנטיים, האנרגיה המינימלית של כל זוג ספינים תהיה כאשר הם מצביעים בכיוונים מנוגדים. בשריג ריבועי, לדוגמא, לספינים אין כל מניעה להסתדר בכיוונים מנוגדים (ראה תמונה 1.1). אך לא כך הסיפור כאשר מסתכלים על שריג משולש. בשריג משולש הסימטריה השריגית לא מאפשרת לכל האינטרקציות המערבות זוגות ספינים להיות מסופקות בו זמנית. כלומר, בשריג משולש, שניים מהספינים יסתדרו בכיוונים מנוגדים ויתירו את הספין השלישי מתוסכל, שכן אינו יכול להיות מנוגד לשני הספינים האחרים בו זמנית (ראה תמונה 1.2). שילוב זה של שריגים המבוססים על שריג משולש ואנטיפרומגנטיות גורם לתופעה של תסכול מגנטי. חומרים המתוסכלים מגנטית אינם יכולים בעת ובעונה אחת למזער את האנרגיה הכללית של מצב היסוד, דבר הסותר את החוק השלישי של התרמודינמיקה. כתוצאה מכך ישנו מצב יסוד מנוון המכיל מספר עצום של מצבים שקולים בעלי אותה אנרגיה. חומרים מתוסכלים מגנטית נקראים 'מגנטיים מתוסכלים'. משפחת המגנטיים המתוסכלים מכילה בתוכה שריגים דו-מימדיים הנקראים 'קגומה', המבוסס על שריג משולשים החולקים קודקודים משותפים (שריג בצורת מגן דוד-ראה תמונה 1.3), והשקול התלת-מימדי שנקרא 'פיירוכלור', המבוסס של טטראדרים החולקים קודקודים משותפים. שריג קגומה בעל אינטראקציות אנטיפרומגנטיות הינו מודל אידאלי המאפשר לחקור את תופעת התסכול המגנטי במימדים נמוכים. במהלך שלושת העשורים האחרונים הושקעו מאמצים רבים במטרה למצוא את הגביש המושלם לחקר

מצב היסוד של שריג קגומה. גביש דו-מימדי בעל ספין $1/2$, ללא אינטראקציות ארוכות טווח וללא זיהומים. החיפוש אחר הגביש המושלם הוליד מספר לא מצומצם של חומרים חדשים.

גביש ה-SCGO בעל הנוסחה המולקולרית $SrCr_xGa_{12-x}O_{19}$, הינו שריג קגומה בעל ספין $3/2$. הערך הגבוה, יחסית, של הספין עלול לגרום לפלאקטואציות קוונטיות חזקות. נמצא כי ל-SCGO מישורי קגומה ומישורי משולשים לסירוגין. בנוסף לכך, אטומי ה-Ga, שאינם מגנטיים, מזהמים את מישורי הקגומה בעקבות החלפת מקומות חלקית עם אטומי ה-Cr המגנטיים.

מועמד נוסף, הינו הוולבורטייט, בעל הנוסחה המולקולרית $Cu_3V_2O_7(OH)_2 \cdot 2H_2O$. זהו שריג דו מימדי בעל ספין $1/2$ המכיל שני אתרים שונים של אטומי Cu דבר הגורם לעיוות במבנה השריגי.

משפחת הג'רוסייט המכילה את $KCr_3(OH)_6(SO_4)_2$, $KFe_3(OH)_6(SO_4)_2$. לשני חומרים אלו ספין השונה מ $1/2$. כמו כן, נמצא כי לג'רוסייט המכיל אטומי ברזל מצב יסוד בעל אינטראקציות ארוכות טווח, אינטרקציה אותה לא מצפים למצוא בשריג קגומה אידאלי. הוסיג'נייט, $BaCu_3V_2O_8(OH)_2$, מועמד נוסף שהוצע לחקר מצב היסוד של גבישי קגומה. הינו בעל ספין $1/2$ כנדרש אך אינו בעל מבנה קגומה מושלם וזיהומים נתגלו בטמפרטורות נמוכות של מדידות מגנטיזציה.

שני חומרים נוספים ופחות נחקרים הם הקאפלאסייט, $Cu_3Zn(OH)_6Cl_2$, וההיידאייט, $Cu_3Mg(OH)_6Cl_2$ אשר נמצאו בהם פגמים במישורי הקגומה.

הרברטסמיטייט, $ZnCu_3(OH)_6Cl_2$, נחשב למימוש הראשון של שריג קגומה מושלם בעל ספין קוונטי $1/2$. אינו מכיל אינטראקציות ארוכות טווח והינו בעל אינטראקציות

אנטיפרומגנטיות חזקות. אולם, ככל שהמחקר על חומר זה העמיק, התגלה כי החומר לא מושלם דיו. נמצא כי מישורי הקגומה מזוהמים כתוצאה מאטומי האבץ בחומר. כ- 10% מאטומי הנחושת במישור החליפו מקומותיהם עם אטומי האבץ אשר נמצאים מחוץ למישור הקגומה. אטומי הנחושת הינם מגנטיים בעוד שאטומי האבץ אינם מגנטיים.

אף לא אחד מכל החומרים הנ"ל מספיק טוב בכדי להיות המימוש המושלם של שריג הקגומה. לאחרונה, חומר חדש בעל סימטריית הקגומה סונתז על ידי קבוצת המחקר באוניברסיטת MIT שבארה"ב. המועמד החדש, $Cu(1,3-bdc)$, הינו אורגנומתכתי המבוסס על נחושת בעלת ספין קוונטי $1/2$. מדידות קרני רנטגן הראו כי חומר זה הוא בעל מבנה קגומה מושלם. בניגוד להרברטסמיטיט, בחומר זה לא קיימים אטומי אבץ, או כל אטום מתכתי אחר, היכולים לגרום לזיהומים במישור הקגומה. מישורי הקגומה מופרדים באמצעות מקשרים-אורגניים, מולקולות בנזן. אטומי הנחושת הינם האטומים המתכתיים והמגנטיים היחידים בחומר, על כן לא, צפויים זיהומים כגון אלו הנראו בחומרים שונים בעבר. מרחקם של אטומי הנחושת, הנמצאים במישורי קגומה מקבילים, ארוך יותר מזה של אטומי נחושת הנמצאים באותו מישור (ראה תמונה 1.4). מכאן ששריג זה יכול לשמש כשריג דו-מימדי. בעבודה זו נחקר את גביש ה- $Cu(1,3-bdc)$ באמצעות מדידות מגנטיזציה ותהודה מגנטית אלקטרונית על מנת לאפיין את ההמילטוניאן של המערכת. כמו כן, נעשו מדידות μSR בכדי לאפיין את מצב היסוד של המערכת.

מדידות הסוספטביליות נערכו בפקולטה לפיסיקה בטכניון במעבדת המחקר של פרופ' עמית קרן, מדידות תהודה מגנטית אלקטרונית נערכו בפקולטה לכימיה במתקן לספקטרוסקופיית תהודה מגנטית גרעינית בטכניון ומדידות μSR נערכו במאיץ חלקיקים בשוויץ, מכון PSI. מדידות מגנטיזציה שנעשו על אבקת ה- $Cu(1,3-bdc)$ מצביעות על התנהגות אנטיפרומגנטית וטמפרטורת קירי-וייס של $-33 K$. אולם, באמצעות אוריינטצית הדגם וחזרה על מדידות מגנטיזציה, שתי טמפרטורות קירי-וייס שונות נתגלו. בהפעלת שדה מגנטי חיצוני המקביל למישור הקגומה, טמפרטורת קירי-וייס מצביע על התנהגות פרומגנטית. בעוד

שהפעלת שדה מגנטי הניצב למישור הקגומה מתקבלת טמפרטורת קירי-וייס עצומה, אשר אינה אמינה אך עם כל זאת כנראה מעידה על התנהגות אנטיפרומגנטית חזקה. מדידות המגנטיזציה מצביעות על כך שהחומר הנבדק, $Cu(1,3-bdc)$, מאוד לא איזוטרופי. מדידות תהודה מגנטית אלקטרונית מחזקות את ההתנהגות האנאיזוטרופית שהתגלתה. בתהודה מגנטית אלקטרונית נמדדת בליעת אנרגיה על ידי אלקטרונים בלתי מזווגים הנמצאים בשדה מגנטי. מדידות אלו מראות כי לחומר זה שני ערכי g שונים, כתלות של הדגם בשדה החיצוני המופעל. כמו כן, קווי הבליעה בספקטרום שהתקבלו הינם בעלי רוחבי-קו שונים, עבור הכיוונים השונים. ערכים אלו אינם תלויי טמפרטורה. מדידות מגנטיזציה ותהודה מגנטית אלקטרונית בשילוב חישובים תאורטיים מאפשרים לקבוע ולאפיין המילטוניאן המתאר את המערכת. מצב היסוד של המערכת נקבע באמצעות מדידות μSR . הרעיון מאחורי טכניקת ה μSR היא למדוד את ההתפתחות בזמן של הספין המיואני בחומר, דבר המתאר את המגנטיות בחומר. ממדידות אלו התגלה כי החל מטמפרטורה של $1.8K$ מתחילה האטה בפלקטאציות הספיניות, כלומר החומר אינו קופא (לפחות עד לטמפרטורה של $50mK$). כמו כן, מדידות אלו מראות על אינטראקציות קצרות טווח אשר אופיניות לשריגי קגומה דו-מימדיים. מתוך כל הניסויים שנערכו ניתן לומר כי $Cu(1,3-bdc)$ הינו מימוש מצויין של שריג קגומה מושלם.

העבודה מסודרת כדלקמן:

- בפרק 1 אנו מסבירים את תופעת המגנטים המתוסכלים ומציגים את כל החומרים שנבדקו עד כה אך לא הניבו תוצאות מספקות.
- בפרק 2 מתאר את המערכות הניסיוניות בהן השתמשנו בכל אחד מהניסויים שנערכו לשם חקירת שריג הקגומה. כמו כן, מוצגות התיאוריות והעקרונות של שיטות המדידה בהן השתמשנו: מדידות מגנטיזציה, תהודה מגנטית אלקטרונית ומדידות μSR .

- בפרק 3 מובאות תוצאות הניסויים. ראשית מוצגות תוצאות ממדידות הסוספטביליות אשר נעשו בטמפרטורות שונות, שדות מגנטיים שונים וכן כתלות באוריינטצית הדגם. לאחר מכן, מוצגות התוצאות ממדידות התהודה מגנטית אלקטרונית, גם הן כתלות באוריינטציית הדגם ביחס לשדה החיצוני המופעל. בסוף פרק זה, מוצגות תוצאות המדידה ממערכת ה- μSR בכל שלושת הקונפיגורציות האפשריות: שדה חיצוני ניצב, אורכי וללא הפעלת שדה חיצוני.

- פרק 4 מציג דיון בתוצאות הניסוי ומקשר בין הניסיון לתיאוריה

- פרק 5 מסכם את העבודה שנעשתה במחקר זה.